Lithos 342–343 (2019) 135–151

Contents lists available at ScienceDirect

Lithos

journal homepage: www.elsevier.com/locate/lithos

Crystal fractionation of contaminated melts and re-melting of newly underplated basaltic crust generated Late Triassic andesitic and dioritic intrusions in the southern Yidun Terrane, SW China

Xin-Song Wang [a,b], Xian-Wu Bi [a,*], You-Wei Chen [a], Li-Chuan Pan [a], Lei-Luo Xu [a]

[a] State Key Laboratory of Ore Deposit Geochemistry, Institute of Geochemistry, Chinese Academy of Sciences, Guiyang 550005, China
[b] Department of Earth and Planetary Sciences, McGill University, 3450 University Street, Montréal, Québec H3A 2A7, Canada

ARTICLE INFO

Article history:
Received 1 December 2018
Accepted 26 May 2019
Available online 30 May 2019

Keywords:
Andesitic intrusion
Dioritic intrusion
MME
Subduction
Crystal fractionation
MASH

ABSTRACT

The genesis of andesitic and dioritic rocks in continental arcs is hotly debated, and proposed models include slab melting, juvenile mafic lower-crustal melting, mafic and felsic magma mixing, and mantle-derived melts that underwent a MASH (melting, assimilation, storage, and homogenization) process. The controversy comes from the possibility of their polygenesis and the ambiguity of bulk-rock isotope tracers, not to mention the processes of magma evolution. Here, we report on our investigations in the southern Yidun Terrane (a Triassic continental arc in SW China) into the petrogenesis of two stages of the dioritic Xiuwacu intrusions (phases 1 and 2), the mafic microgranular enclaves (MMEs) hosted by the phase 1 intrusion, as well as the andesitic Hongshan intrusions. We used U-Pb zircon dating, in situ zircon Hf-O isotope analyses, bulk-rock Sr-Nd isotope analyses, and trace element analyses of the zircons from different stages of the intrusions and the MMEs to shed light on their sources and mantle–crust interactions involved in their petrogenesis. Our results suggest that the Xiuwacu MMEs from the phase 1 intrusion crystallized from a melt. Their variable zircon Hf-O isotopic compositions ($\varepsilon Hf(t) = +0.4$ to $+5.3$ and $\delta^{18}O = 4.80‰$ to 7.79‰) indicate they were formed by the mixing of mantle-derived basaltic melts and felsic melts. The phase 1 intrusion have an origin similar to that of the MMEs, as indicated by their homogeneous zircon Hf-O isotopic compositions ($\varepsilon Hf(t) = +1.3$ to $+3.9$ and $\delta^{18}O = 6.58‰$ to 7.31‰), which fall within the range of the isotopic compositions of the MMEs. The discovery of several inherited zircons and a small recrystallized felsic microgranular enclave hosted by an MME reveals that the MMEs contain relatively more felsic components. Even so, the MMEs still have lower silica contents (62.1–63.4 wt%) than those of the phase 1 intrusion (63.4–70.5 wt%), and this indicates that direct magma mixing of basaltic and felsic melts generated the andesitic MMEs, whereas a crystal fractionation process is required for the dioritic phase 1 intrusion. The porphyritic phase 2 and Hongshan intrusions formed at ~216 Ma, after the phase 1 intrusion, and they had higher oxygen fugacities and crystallization temperatures than the phase 1 intrusion. Given the conclusions of previous researchers that slab breakoff probably occurred at ~216 Ma, we propose that the Xiuwacu phase 2 and Hongshan intrusions formed during the slab breakoff process, the former by partial melting of the newly underplated basaltic lower crust in the MASH zone, and the latter by differentiation of mantle-derived basaltic melts at relatively high pressures.

1. Introduction

Andesitic and dioritic intrusions are among the principal components of continental arcs, and they host numerous porphyry copper deposits around the world (Lee and Bachmann, 2014). Studying the genesis of andesitic and dioritic igneous rocks in continental arcs helps us to understand mantle–crust interactions in subduction zones and the generation of mineral resources (Lee and Bachmann, 2014; Richards, 2003; Stern, 2002). Several models have been proposed to explain the genesis of these rocks in convergent margins, including slab melting (Defant and Drummond, 1990), basaltic lower-crustal melting (Atherton and Petford, 1993; Hansen et al., 2002), mixing of mafic and felsic melts (Barnes et al., 2012), and partial melts of the hydrous mantle wedge undergoing the processes of MASH (melting, assimilation, storage, and homogenization) or AFC (assimilation and fractional crystallization) within the lower crust (Chiaradia, 2009; Hildreth and Moorbath, 1988; Lee and Bachmann, 2014; Richards, 2003). Although these various models have distinguishing characteristics, it is difficult to distinguish them from each other using traditional methods,

* Corresponding author at: State Key Laboratory of Ore Deposit Geochemistry, Institute of Geochemistry, Chinese Academy of Sciences, Guiyang 550005, China.
E-mail addresses: wangxinsong@mail.gyig.ac.cn (X.-S. Wang), bixianwu@vip.gyig.ac.cn (X.-W. Bi).

https://doi.org/10.1016/j.lithos.2019.05.033
0024-4937/

including bulk-rock geochemistry and radioisotope tracers. For example, slab-derived melts, mafic lower-crustal melts, and fractionated hydrous mantle melts under high pressure all have high Sr/Y ratios. Whole-rock isotope analyses alone cannot distinguish between end-members with similar isotopic compositions, and enriched mantle (EM1 and EM2), for example, has whole-rock Sr–Nd–Pb isotopic compositions similar to those of older continental crust and some juvenile crust (Lee and Bachmann, 2014; Litvinovsky et al., 2015). In addition, whole-rock isotope compositions commonly reveal mixed information, and may be homogenized during the mixing of mafic and felsic magmas (Li et al., 2009).

In contrast, in situ zircon Hf-O isotope analyses can be used to constrain the magma sources. Mantle-derived magmas have a narrow range of zircon oxygen isotopic values (5.0‰–6.5‰), and supracrustal-contamination of these magmas would have raised the values to >6.5‰ (Valley et al., 2005). Combined with in situ zircon Hf isotopic analyses, such data provide effective constraints that can be used to trace young or old continental and oceanic crustal-derived melts (Wang et al., 2014b; Wang et al., 2016; Zhu et al., 2017). Mafic microgranular enclaves (MMEs) are commonly present in andesitic and dioritic intrusions (Barbarin and Didier, 1992), and investigating the genesis of the different stages of the intrusions and their MMEs with in situ zircon Hf-O isotope analyses can reveal their petrogenesis and the processes of interaction between mantle and crust (Kemp et al., 2007; Lu et al., 2013; Pietranik et al., 2013). In addition, investigations of the trace elements of the zircons can be used to constrain the chemical-physical conditions of crystallization of the intrusions, which helps in understanding the genesis of the magmas.

The southern Yidun Terrane is a Triassic continental arc that formed during the westwards subduction of the Ganzi–Litang oceanic crust. Large volumes of andesitic and dioritic intrusive material as well as several large porphyry Cu deposits occur along the arc. The genesis of these intrusions is hotly debated. It has been proposed that they were derived from slab melting (Wang et al., 2011; Wang et al., 2018), melting of juvenile mafic lower crust (Cao et al., 2016), mixing of mafic and felsic magmas (Leng et al., 2014; Leng et al., 2018), or MASH or AFC processes in mantle-derived melts within the lower crust (Kong et al., 2016).

Two clear stages of intrusive activity can be observed in the southern Yidun Terrane, as for example in the Pulang, Xuejiping, and Disuga areas (Kong et al., 2016; Leng et al., 2018; Wang et al., 2011; Wang et al., 2018). The rocks of the first stage are slightly more felsic (dioritic) and porphyritic, and some host veinlet mineralization. The rocks of the second stage are slightly more mafic (andesitic–dioritic) and porphyritic, and these rocks rarely host veinlet mineralization. However, the genesis of these two stages of intrusive activity is unclear and controversial. Some researchers have proposed that the first-stage intrusions were derived from the partial melting of a subducting slab, and that the later-stage intrusions were formed from a mantle wedge that had been metasomatized by ascending slab melts (Wang et al., 2011; Wang et al., 2018). On the other hand, Leng et al. (2018) argued that the later-stage intrusions were formed by the mixing of mafic and felsic melts. This controversy is compounded by the possibility of polygenesis, the ambiguity of isotope tracers, and not taking the evolution of the magmas into consideration. In addition, little attention has been paid to the genesis of the MMEs, and we note in particular that the use of in situ zircon Hf-O isotope analyses would almost certainly provide useful information on magma sources and petrogenesis.

The Xiuwacu intrusions in the southern Yidun Terrane consist of two phases of dioritic intrusion with clear intrusive contacts and different textures, and numerous large MMEs are hosted by the first phase of these intrusive rocks. The Hongshan intrusion is andesitic and good candidate for our study. In this paper, we present the results of our investigation into the two phases of the Late Triassic Xiuwacu intrusions and their MMEs, as well as the results of our investigation into the Hongshan intrusion in the southern Yidun Terrane. Highly precise U-Pb zircon ages and O isotope data were obtained using secondary ionization mass spectrometry (SIMS), Hf isotope compositions were obtained for these intrusive igneous rocks using LA–MC–ICP–MS, and whole-rock Sr-Nd isotopic and geochemical data for these rocks and their MMEs are presented to constrain their petrogenesis. We found that in situ zircon Hf-O isotope and trace element data for the different stages of these intrusive rocks and their MMEs, as well as understanding the chemical–physical conditions of crystallization, provide good constraints on the genesis and evolution of these arc magmas.

2. Geological setting

The Yidun Terrane is located between the Qiangtang Terrane (to the west), the Songpan–Ganzi Fold Belt (to the northeast), and the Yangtze Craton (to the southeast). It is bounded to the west by the Jinshajiang Suture and to the east by the Ganzi–Litang Suture (Fig. 1a, b; Yin and Harrison, 2000). The terrane is made up of two parts, the Zhongza Massif (the western Yidun Terrane) and the eastern Yidun Terrane (Reid et al., 2007), which are separated by the north–south trending Xiangcheng–Geza fault zone. The Zhongza Massif is inferred to be a microcontinent that separated from the Yangtze Craton in the late Permian during the opening of the Ganzi–Litang Ocean (Chang, 1997). The Zhongza Massif consists of Paleozoic metasedimentary rocks, which are the oldest rocks exposed in the Yidun Terrane. These carbonate-rich Paleozoic successions have fossil assemblages similar to those of the sediments and metasediments of the Longmen Shan Thrust Nappe Belt, in the west of the Yangtze Block (Chang, 1997), which indicates that the Zhongza Massif separated from the Yangtze Block. The zircons in these sedimentary rocks have the same peak ages as detrital zircons from the western Yangtze Block (Wang et al., 2013a). All of this evidence suggests that the Yidun Arc has the same crystalline basement as the Yangtze Block.

The eastern Yidun Terrane consists of north–south trending Triassic flysch–volcanic successions of the Yidun Group and Late Triassic intrusions that formed as a result of the westwards subduction of the Ganzi–Litang oceanic crust beneath the Zhongza Massif (Hou et al., 2003; Leng et al., 2012; Wang et al., 2011; Wu et al., 2017). The eastern Yidun Terrane can be divided into the northern Yidun Terrane (in the Changtai and Xiangcheng regions) and the southern Yidun Terrane (in the Shangri–La region) on the basis of the distinctive nature of the Triassic and Cretaceous magmatism and mineralization in these two terranes (Hou et al., 2003; Wang et al., 2014b).

In the northern Yidun Terrane, large volumes of common andesite and back-arc sedimentary strata are distributed along the north–south axis of the terrane in the Changtai and Xiangcheng areas. In addition, a Triassic bimodal volcanic suite formed alongside the andesites in the Changtai area. The bimodal volcanic suite has been dated at ~230 Ma, and the basalts in the suite have back-arc basalt affinities (Wang et al., 2013b). The northern Yidun Terrane is also characterized by the presence of large batholiths of barren granitoid located between the volcanic rocks and the Ganzi–Litang Suture Zone. These granitoid batholiths are 225 to 215 Ma in age, they have I-type granite affinities, and they were formed by the mixing of magmas derived from the mantle and metasedimentary rocks (He et al., 2013; Wu et al., 2017). Wu et al. (2017) reported the presence of several ~230 Ma Middle Triassic intrusions in the Changtai area. Together with the U-Pb zircon ages of the Late Triassic igneous rocks in the northern Yidun Terrane, the age data show that there were three periods of magmatism at ~230, ~225, and ~216 Ma. In the early stages from ~235 to ~220 Ma, the magmas were mainly related to the subduction of the Ganzi–Litang oceanic crust (Hou et al., 2003; Hu et al., 2005; Reid et al., 2007; Wang et al., 2013a; Wang et al., 2013b; Weislogel, 2008; Wu et al., 2017), but it has been suggested that the late stage ~216 Ma magmatism was triggered by slab breakoff (Wang et al., 2011; Wang et al., 2013a; Wang et al., 2013b; Wu et al., 2017). The occurrence of Jurassic igneous intrusions in the Yidun Terrane and the Songpan–Ganzi Fold Belt is generally considered to be an indicator of the post-orogenic environment that existed

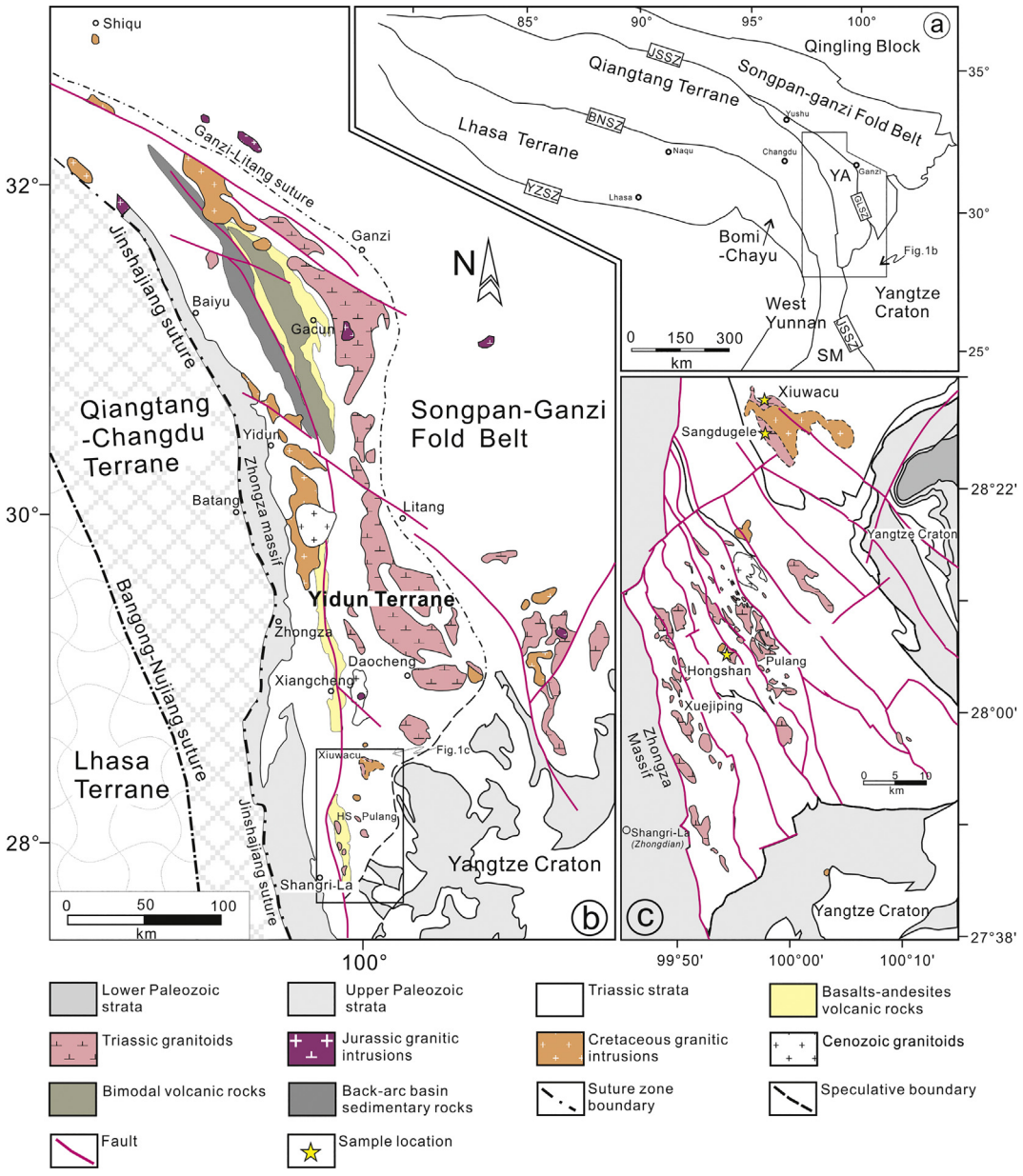

Fig. 1. (a) Regional map showing the terranes and Mesozoic granitoids of the Tibetan Plateau. (b) Simplified geologic map of the Yidun Terrane. (c) Simplified geologic map of the Shangri–La region (modified after Wang et al., 2014b). Abbreviations: JSSZ = Jinsha Suture Zone; GLSZ = Ganzi–Litang Suture Zone; BNSZ = Bangong–Nujiang Suture Zone; YZSZ = Yarlung–Zangbo Suture Zone; YA = Yidun Terrane (or Yidun Arc); HS = Hongshan.

after the collision of the two terranes (Hu et al., 2005; Qu et al., 2003; Wang et al., 2008). A belt of Cretaceous A-type granites is located in the Baiyu–Batang region (Fig. 1b; Hou et al., 2003).

In contrast, in the southern Yidun Terrane, a narrow belt of basaltic–andesitic volcanic rocks and porphyritic intrusions is associated with porphyry-type or skarn-type Cu mineralization, including the Pulang and Xuejiping porphyry Cu deposits (Fig. 1b; Hou et al., 2003; Li et al., 2011; Leng et al., 2012). The volcanic rocks range in age from 220 to 216 Ma, and they have high Sr/Y (28–102) and La/Yb (22–42) ratios (Leng et al., 2014; Wang et al., 2011). These Late Triassic porphyritic intrusive rocks are high-K calc-alkaline with relatively high values of $\varepsilon_{Nd}(t)$ (−3.8 to −2.1) and $\varepsilon_{Hf}(t)$ (−3.5 to 3.2) and ages ranging from 206 to 230 Ma (Leng et al., 2012; Leng et al., 2014; Leng et al., 2018; Wang et al., 2011). In addition, there are clearly two stages of intrusive activity in the southern Yidun Terrane, as for example in the Pulang, Xuejiping, and Disuga areas (Kong et al., 2016; Leng et al., 2018; Wang et al., 2011; Wang et al., 2018). The rocks of the first stage are porphyritic, slightly more felsic (dioritic), and some host veinlet mineralization. The rocks of the later stage are slightly more mafic (andesitic–dioritic), have typical porphyritic textures, and rarely host any mineralization. Wang et al. (2011) proposed that the early stage porphyritic intrusions formed as a result of the partial melting of a dipping slab, whereas the late stage intrusions formed by the partial melting of a mantle wedge that had been metasomatized by slab-melts during a process of slab breakoff. In addition, several Late Cretaceous adakitic intrusions (Fig. 1b) indicate an intra-plate transtensional environment that was triggered by the collision of the Lhasa and Qiangtang terranes (Wang et al., 2014a; Wang et al., 2014b; Wang et al., 2015; Yang et al., 2016).

3. Petrography and sampling

The samples for our study were collected from the Xiuwacu pluton and the Hongshan intrusions. The Xiuwacu pluton is located 80 km northeast of Shangri–La (Zhongdian) City (Fig. 1c), and it is made up

of Late Triassic and Late Cretaceous intrusions. The petrology of the Late Cretaceous intrusive rocks has been described in detail in a previous paper (Wang et al., 2014b). The Late Triassic intrusions are distributed in the outer zones of the Xiuwacu pluton, including the Xiuwacu zone in the north and the Sangdugele zone in the south (Fig. 1c). Based on our field observations, the Xiuwacu Late Triassic granites can be divided into two phases of intrusive activity. Phase 1 intrusion contain early medium–coarse grained quartz monzonites and granites (Fig. 2a, d). Phase 2 intrusion contain later quartz monzonitic porphyries (Fig. 2b, e). There are distinct intrusive contacts between the phase 2 and phase 1 rocks (Fig. 2g), and on the phase 1 side of the contact there was baking with the original gray color changed to white. This indicates that the phase 1 intrusive rocks had already cooled to low temperatures before the phase 2 magmas were emplaced. In addition, mafic microgranular enclaves (MMEs) of various size (5–40 cm) are widespread in the phase 1 intrusive rocks, and the MMEs have sharp contacts with the host rocks (Fig. 2g). The strata in the Xiuwacu area consist of Late Triassic medium-layered sandstones and slates.

The phase 1 intrusive rocks are gray, medium–coarse grained, and made up of 5%–10% amphibole, 30%–35% K-feldspar, 20%–25% plagioclase, 15%–25% quartz, 10%–15% biotite, and accessory zircon, apatite, magnetite, and titanite (Fig. 2a, b). The phase 2 intrusive rocks are dark and porphyritic, and they consist of ~20% K-feldspar, ~30% plagioclase, ~15% quartz, 5%–15% biotite, 1%–5% amphibole, and accessory zircon, apatite, magnetite, and titanite. The phenocrysts are plagioclase, biotite, and amphibole (Fig. 2e, f). The MMEs in the phase 1 intrusion consist of ~10%–20% amphibole, ~15% K-feldspar, ~25% plagioclase, 10%–20% quartz, 15%–20% biotite, and accessory zircon, apatite, magnetite, and titanite (Fig. 2h, j, k). In addition, these MMEs host small felsic microgranular enclaves (FME) that consist of biotite, quartz, plagioclase, and K-feldspar, but do not contain amphibole (Fig. 2i–k). The FMEs have a recrystallized texture characterized by preferred orientations of

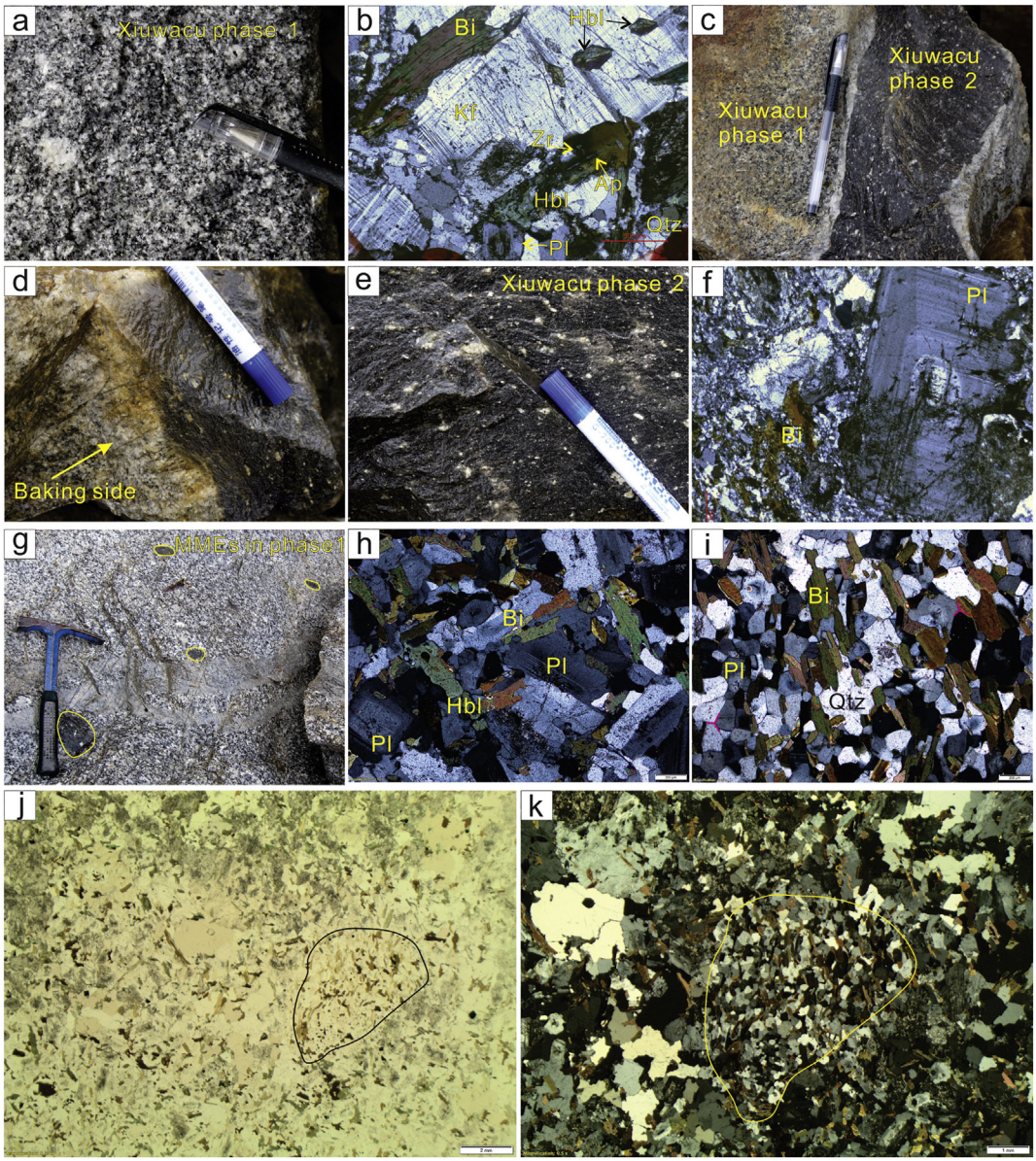

Fig. 2. Field photographs and photomicrographs of the Late Triassic intrusive rocks in the Xiuwacu area. (a) and (b) Xiuwacu phase 1 quartz monzonite. (c) Xiuwacu phase 2 intruded into Xiuwacu phase 1. (d) The baked side of the phase 1 material was heated and lost color during the intrusion of the hot melt of phase 2. (e) and (f) Xiuwacu phase 2 intrusive rock. (g–k) Mafic microgranular enclaves (MMEs) in the phase 1 intrusion. (h) Photomicrograph of an MME showing the texture with euhedral and subhedral plagioclase, biotite, and amphibole. (i) Felsic microgranular enclave (FME) from a MME. The FME exhibits recrystallization textures, and consists of biotite, quartz, plagioclase, and K-feldspar, but without amphibole. (j) and (k) The FME was hosted by the MME, and the FME has an unclear or blurry contact with the MME. Mineral abbreviations: Kf = K-feldspar, Bi = biotite, Hbl = hornblende, Pl = plagioclase, Qtz = quartz, Zr = zircon, and Ap = apatite.

biotite and 120° angles at the boundaries between the other minerals. The FMEs have unclear or blurry contacts with the MMEs.

The Late Triassic Hongshan monazite intrusions contain 25%–40% phenocrysts and 75%–60% matrix. The phenocrysts are 15%–20% plagioclase, 10%–15% amphibole, ~5% biotite, and 0%–5% quartz, and the accessory minerals are zircon, apatite, magnetite, and titanite.

For our study, we collected samples from the Late Triassic Xiuwacu phase 1 and phase 2 intrusions in the outer zones of the Xiuwacu pluton, including the Xiuwacu (north) and Sangdugele (south) zones (Fig. 1c). The samples from the Late Triassic Hongshan intrusions were collected from the Hongshan area. All the samples were fresh, except for minor local alteration of feldspar to sericite.

4. Analytical methods

4.1. U-Pb Zircon dating

Zircons were separated from the samples using conventional heavy liquid and magnetic separation techniques. Representative zircon grains were hand-picked under a binocular microscope and mounted in an epoxy resin disk, and then polished to about half their thickness for analysis. The zircons were documented with transmitted and reflected light photomicrographs as well as cathodoluminescence (CL) images to reveal their internal structures (Fig. 3). Measurements of U, Th, and Pb isotopes were conducted using a Cameca IMS 1280 large-radius SIMS at the Institute of Geology and Geophysics (IGG), Chinese Academy of Sciences (CAS), Beijing. The analytical procedures used were the same as those described by Li et al. (2009). The O^{2-} primary ion beam was accelerated at 13 kV with an intensity of ~8 nA. The ellipsoidal analytical spots were about 20 × 30 μm in size. Positive secondary ions were extracted using a 10 kV potential. Each measurement consisted of 7 cycles, and the total analytical time was ~12 min. Analyses of the unknown samples were interspersed with analyses of standard zircon Qinghu, for which the U–Th–Pb isotope ratios were calibrated relative to its standard recommended U-Pb age of 159.5 ± 0.2 Ma (Li et al., 2009). The results for standard zircon Qinghu, as determined by us, are listed in Appendix 1 and Fig. 3. The measured compositions were corrected for common Pb using the measured non-radiogenic ^{204}Pb. Uncertainties on individual analyses are reported at the 1σ level, and the weighted mean ages of the pooled U-Pb analyses are quoted with a 95% confidence interval. Data reduction was carried out using the Isoplot program of Ludwig (2003).

4.2. Zircon O isotope analyses

The zircon samples analyzed for their O and Hf isotope contents were collected from each of the phases of intrusive rock in the Xiuwacu pluton and from various Hongshan intrusions. The rock samples included a biotite granitic porphyry (Xiuwacu phase 1 intrusion, XS12-17), a monzogranite (Xiuwacu phase 2 intrusion, XS12-07), an MME (XWC11-42), and a granitic porphyry (Hongshan, HS11-114).

Zircon oxygen isotopes were measured using the Cameca IMS-1280 SIMS at the IGG, CAS, Beijing. Details of the analytical procedures used are described by Li et al. (2009). A Cs^+ primary ion beam was used as the ion source. The analytical spot sizes were about 20 μm in diameter. Oxygen isotopes were measured using the multi-collection model on two off-axis Faraday cups. Each analysis took ~4 mins. The uncertainty of an individual analysis was usually <0.2‰ (1σ) (Li et al., 2009). The instrumental mass fractionation factor was corrected using zircon Penglai and the Qinghu standard with $\delta^{18}O$ values of 5.31 ± 0.10‰ (2SD) and 5.4 ± 0.2‰ (2SD), respectively (Li et al., 2009; Li et al., 2010). Our analytical results for standard zircons Qinghu and Penglai are listed in Appendix 2.

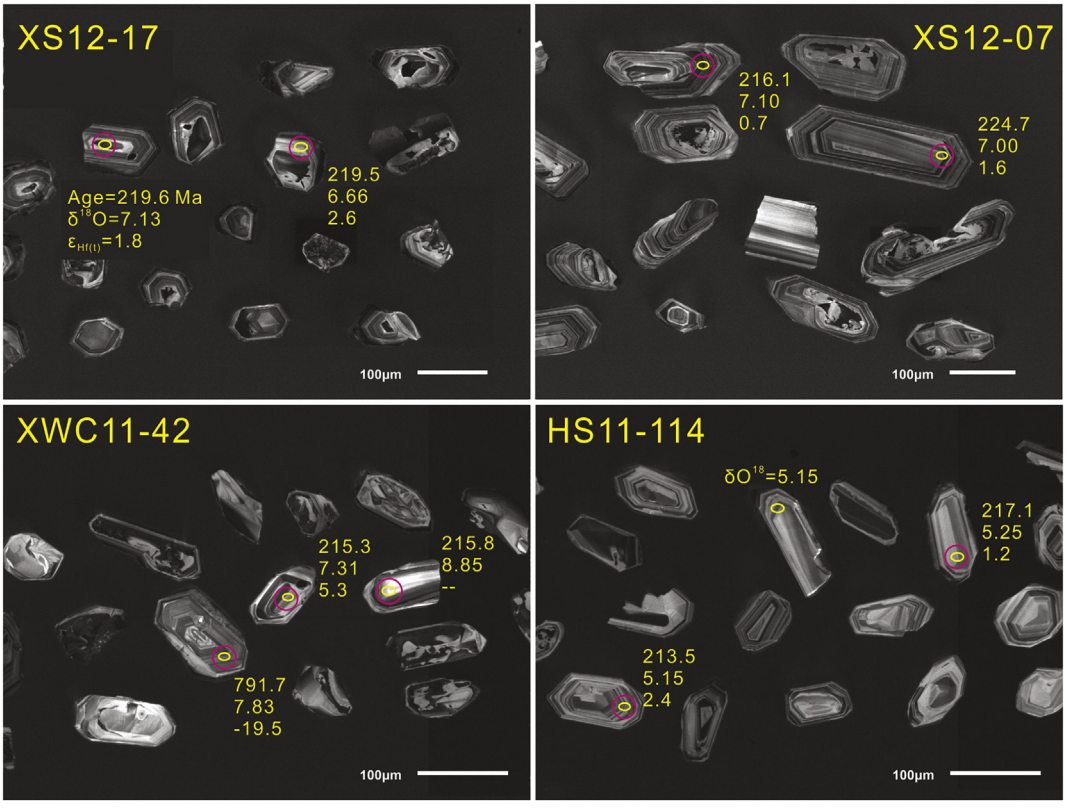

Fig. 3. CL images of representative zircons analyzed for their in situ Hf and O isotope compositions. The small ellipses indicate the SIMS analytical spots for U-Pb ages and O isotopes, and the big circles denote the LA–MC–ICPMS analytical spots for Hf isotopes. The numbers near the analytical spots are the age, $\delta^{18}O$, and εHf(t) values, from top to bottom.

4.3. Zircon Hf isotope analyses

The zircon Lu-Hf isotope analyses were conducted using a Neptune Plus MC–ICP–MS equipped with a Geolas 2005 excimer ArF laser ablation system at the State Key Laboratory of Geological Processes and Mineral Resources, China University of Geosciences, Wuhan. A wire signal smoothing device was included in the laser ablation system, allowing for the production of smooth signals even at very-low laser repetition rates (down to 1 Hz) (Hu et al., 2012a). The laser ablation energy density used in this study was 5.3 J/cm^2. Helium was used as the carrier gas within the ablation cell and was merged with argon (makeup gas) after the ablation cell. For the 193 nm laser, a consistent 2-fold signal enhancement was achieved using helium rather than argon gas (Hu et al., 2012a). A simple Y junction downstream from the sample cell was used to add small amounts of nitrogen (4 ml/min) to the argon makeup gas flow. All our data were acquired on zircons in single spot ablation mode with analytical spot sizes of 44 μm. Each measurement consisted of 20 s of acquisition of the background signal followed by 50 s of ablation signal acquisition. Details of the operating conditions used for the laser ablation system and the MC–ICP–MS instrument, as well as the analytical methods, have been described by Hu et al. (2012b). Our determined $^{176}Hf/^{177}Hf$ ratios of 0.282309 ± 0.000024 (2σ, $n = 20$) for zircon standard 91,500 are consistent with the reported $^{176}Hf/^{177}Hf$ ratios of 0.282306 ± 0.000010 (2σ) (Woodhead et al., 2004).

4.4. Whole-rock major and trace element analyses

Fresh rock samples were crushed and then powdered in an agate mill to a grain size of <200 mesh. The concentrations of the major elements were determined using an X-ray fluorescence spectrometer (XRF) at the ALS Chemex (Guangzhou) Co. Ltd., using fused glass pellets created using a mixture of lithium tetraborate and 0.7 g of powdered sample. The analytical precision was better than 5%. Trace element concentrations were analyzed using an Agilent 7700e ICP–MS at the State Key Laboratory of Ore Deposit Geochemistry (SKLODG) in the Chinese Academy of Sciences. Approximately 50 mg of each powdered sample was dissolved in a mixture of 1 ml HF and 1 ml HNO_3. The dissolution step was conducted at 190 °C in a high-pressure Teflon autoclave for 48 h. After cooling, the bombs were opened, 1 ml of 1 ppm Rh solution was added as an internal standard, the capsules were placed on a hot plate (at about 150 °C), and the solutions were evaporated to dryness. One milliliter of HNO_3 was added, evaporated to dryness, followed by a second addition of HNO_3, and then evaporated to dryness again. The final residue was re-dissolved in 8 ml of 40% HNO_3. The bombs were resealed, placed in an oven, and heated at 110 °C for 12 h. After cooling, the final solution was diluted to 100 ml with distilled de-ionized water. Further details of the analytical methods we used can be found in Qi et al. (2000). The analytical precision was better than 10%.

4.5. Whole-rock Sr and Nd isotope analyses

Whole-rock Sr-Nd isotopic compositions were obtained using a Finnigan Triton thermal ionization mass spectrometer (TIMS) at the China University of Geosciences, Wuhan, and the Laboratory of Geoanalysis and Geochemistry, Tianjin. Sample dissolution and Sr-Nd separation and purification were carried out in a clean laboratory. Powdered samples (<200 mesh, ~50 mg each) were dissolved in Teflon bombs using 1 ml of double distilled HNO_3 and 1 ml of HF at 190 °C for 48 h. After cooling, the solutions were dried on a hot plate at 115 °C. The sample residues were re-dissolved in 1–2 ml of 6 N HCl, and then evaporated to dryness. Finally, the samples were dissolved in 1 ml of 2.5 N HCl and centrifuged to remove any remaining undissolved material. The Sr and Nd were separated and purified by successively using ion exchange columns of a AG50W-X12 cation resin and LN-Spec resin. The $^{87}Sr/^{86}Sr$ and $^{143}Nd/^{144}Nd$ ratios were normalized to $^{88}Sr/^{86}Sr = 8.3752$ and $^{146}Nd/^{144}Nd = 0.7219$, respectively. The ratios of $^{87}Sr/^{86}Sr$ for Sr standard NBS987 and $^{143}Nd/^{144}Nd$ for Nd standard JNdi-1 were determined to be 0.710250 ± 0.000010 (n = 6) and 0.512116 ± 0.000006 (n = 3), respectively, during our analytical work. The analytical precision and accuracy were better than 0.01‰ compared to the recommended $^{87}Sr/^{86}Sr$ and $^{143}Nd/^{144}Nd$ values of the standards (0.710251 and 0.512115, respectively; Tanaka et al., 2000; Li et al., 2015). The total procedural blanks were Rb = 3×10^{-11}, Sr = 1.2×10^{-10}, Sm = 3×10^{-11}, and Nd = 1.2×10^{-10}.

4.6. Zircon trace element analyses, magma oxygen fugacities, and crystallization temperature calculations

Trace element analyses of the zircons were conducted using LA–ICP–MS at the State Key Laboratory of Ore Deposit Geochemistry in the Institute of Geochemistry at the Chinese Academy of Sciences. Laser sampling was performed using a *GeoLas Pro* 193 nm ArF excimer laser. An Agilent 7500× ICP–MS instrument was used to acquire the ion-signal intensities. Helium was used as the carrier gas, which was mixed with Argon via a T-connector before entering the ICP–MS. Each analysis incorporated a background acquisition of approximately 30 s (gas blank) followed by 60 s of sample data acquisition. Off-line selection and integration of the background and analyte signals, time-drift corrections, and quantitative calibration for trace element analyses were performed using ICPMSDataCal (Liu et al., 2008, 2010). Zircon 91,500 was used as the external standard and was analyzed twice every 6–8 analyses. The uncertainty of the preferred values for external standard 91,500 was propagated to the ultimate results of the samples. The trace element compositions of the zircons were calibrated using multiple-reference materials (NIST 610, BHVO-2G, BCR-2G, and BIR-1G) and Si internal standardization. The preferred values of the element concentrations used for the USGS reference glasses were obtained from the GeoReM database (http://georem.mpch-mainz.gwdg.de/). A total of 57 major and trace elements were analyzed. The elements of interest included Si, Zr, Ti, La, Ce, Pr, Nd, Sm, Eu, Gd, Tb, Dy, Ho, Er, Tm, Yb, Lu, Y, Pb, Th, U, P, Hf, Sr, and Nb. The detection limits for such elements were from 0.01–0.1 ppm, except for Gd and Sm, which had detection limits of 0.3 ppm. Analyses of NIST610 as the unknown were consistent with the recommended values within 5%.

The oxygen fugacity (fO_2) of the magma was calculated using the Ce anomalies of the zircons as follows:

$$\ln\left(\frac{Ce}{Ce^*}\right)_D = (0.1156 \pm 0.0050) \times \ln(fO_2) + \frac{13,860 \pm 708}{T(K)} - 6.125 \pm 0.484 \quad (1)$$

where $\left(\frac{Ce}{Ce^*}\right)_D$ is the Ce anomaly of the zircon calculated using the partition coefficients, and T is the zircon crystallization temperature in K. The zircon/melt partition coefficients for La, Ce, and Pr were calculated using the La, Ce, and Pr contents of the zircon divided by those of the whole rock (Trail et al., 2012). The zircon crystallization temperature $T(K)$ in Eq. (1) was calculated as follows:

$$\log(Ti_{zircon}) = (6.01 \pm 0.03) - \frac{5080 \pm 30}{T(K)} \quad (2)$$

where Ti_{zircon} is the Ti content of the zircon (Watson et al., 2006).

5. Results

5.1. U-Pb zircon ages

Most of the zircons from samples XS12-17, XS12-07, and HS11-114 from the Shangri–La region are colorless and euhedral with igneous oscillatory zoning. Most of the zircons from sample XWC11-42 are dark and have planar zoning and resorption zoning. Several zircons from sample XWC11-42 have cores of inherited oscillatory zoned zircon

and overgrowths of weakly zoned zircon, the rest of the zircons are euhedral with igneous oscillatory zoning. The zircon grains vary mainly from 60 to 300 μm in length and have length to width ratios of 2:1 to 3:1. The analytical results for the four samples and the standard zircon Qinghu are given in Appendix 1.

Eleven analyses of zircons from sample XS12-17 yielded $^{206}Pb/^{238}U$ ages varying from 215.2 to 232.6 Ma with a weighted mean $^{206}Pb/^{238}U$ age of 220.7 ± 3.4 Ma (2σ, MSWD = 2.4) (Fig. 4a). Eighteen analyses of zircons from sample XS12-07 yielded $^{206}Pb/^{238}U$ ages ranging from 212.9 to 224.7 Ma with a weighted mean age of 217.5 ± 1.5 Ma (2σ, MSWD = 1.0) (Fig. 4b). Twenty-four analyses of zircons from sample XWC11-42 were obtained. The $^{206}Pb/^{238}U$ ages of those zircons with igneous oscillatory zoning varied from 210.3 to 218.7 Ma with a weighted mean age of 213.9 ± 1.7 Ma (2σ, MSWD = 0.5) (Fig. 4c, d). It is slightly younger than the age of phase 1 (XS12-17), which probably indicates a lead loss. The $^{206}Pb/^{238}U$ ages of the inherited core zircons varied from 415.1 to 1484.7 Ma, while the $^{207}Pb/^{206}Pb$ ages of the inherited core zircons varied from 467.0 to 1862.7 Ma (Fig. 4c), with five age peaks at 428–492, 534–643, ~817, ~1237, and ~1858 Ma. Eighteen analyses were conducted on zircons from sample HS11-114. Their $^{206}Pb/^{238}U$ ages ranged from 211.9 to 218.8 Ma with a weighted mean age of 216 ± 1.5 Ma (2σ, MSWD = 0.72) (Fig. 4e).

5.2. Zircon O isotopes

Eighty-two in situ O analyses were conducted on zircons from the phase 1 and 2 intrusions and MMEs in the Xiuwacu area, and from the Hongshan intrusions. These data are given in Appendices 2 and 3. The zircons from the phase 1 intrusion have $\delta^{18}O$ values ranging from 6.58‰ to 7.31‰ with a weighted mean value of 7.04 ± 0.1‰ (2σ) (Fig. 5). The zircons from the phase 2 intrusion have relatively homogenous $\delta^{18}O$ values ranging from 6.73‰ to 7.41‰ with a weighted mean value of 7.04 ± 0.1‰ (2σ) (Fig. 5). The zircons from the MMEs with ages from 210.3 to 218.7 Ma have a wider range of $\delta^{18}O$ values from 4.8‰ to 7.79‰ (Fig. 5), while the zircons with inherited cores have a wider range of $\delta^{18}O$ values from 7.83‰ to 11.5‰. The zircons from the Hongshan intrusions have $\delta^{18}O$ values between 5.11‰ and 6.07‰ with a weighted mean value of 5.51 ± 0.1‰ (2σ) (Fig. 5).

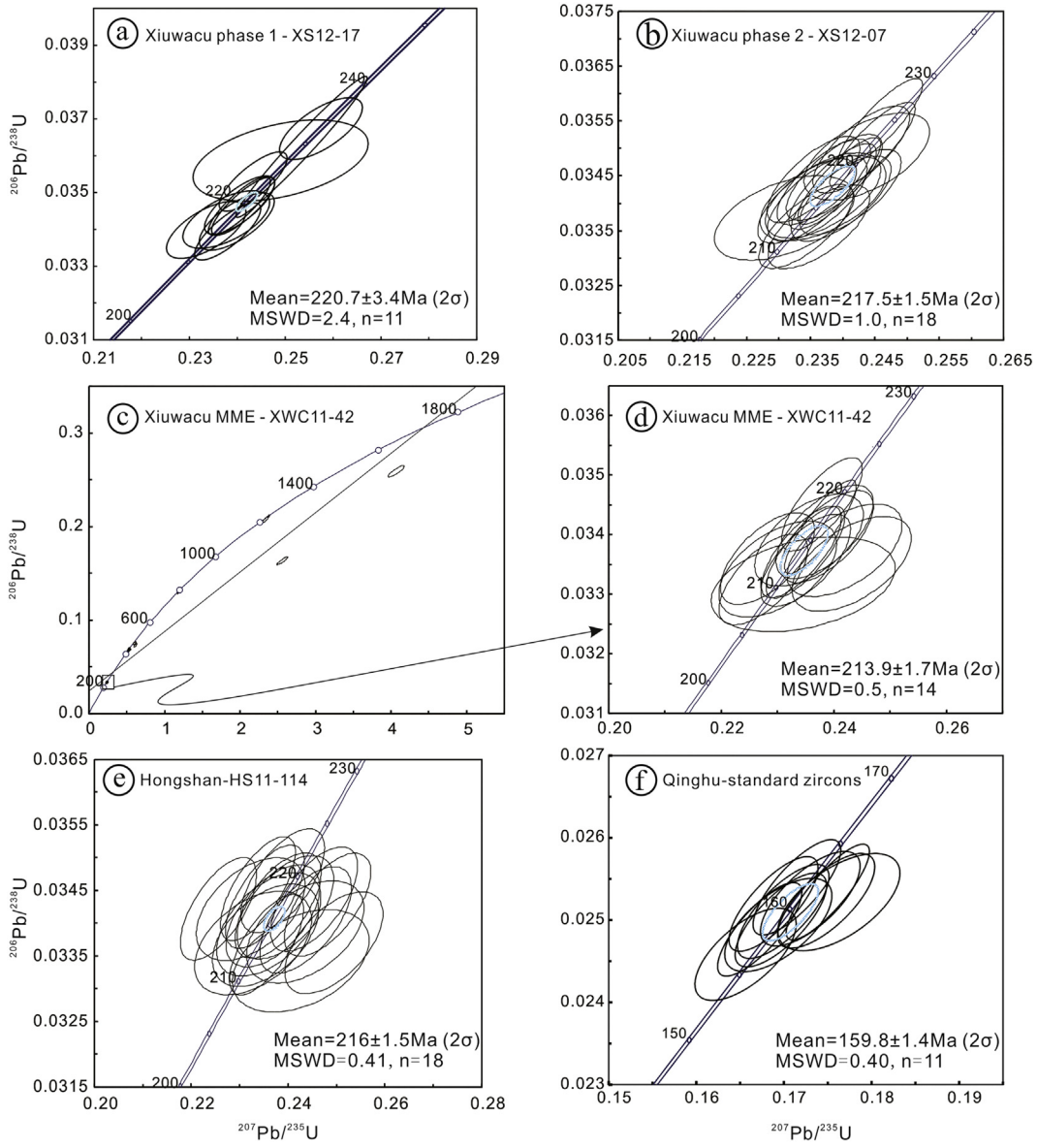

Fig. 4. U-Pb concordia diagrams for zircons from samples of (a) Xiuwacu phase 1 intrusive rocks, (b) Xiuwacu phase 2 intrusive rocks, (c) MMEs in the phase 1 rocks (with the ages of the inherited cores), (d) MMEs in the phase 1 rocks (no inherited core ages), (e) Hongshan intrusive rocks, and (f) the Qinghu standard.

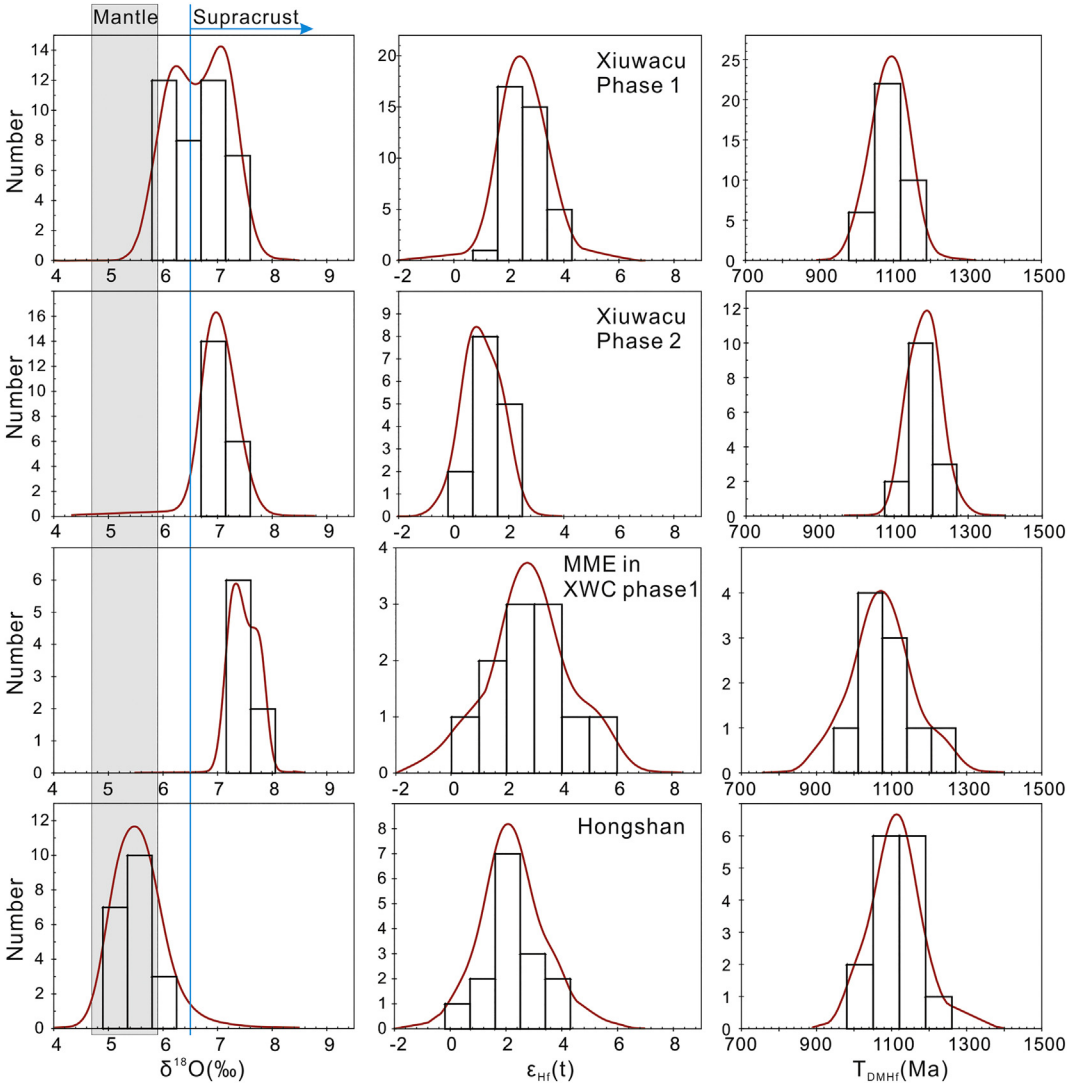

Fig. 5. Histograms of the $\delta^{18}O$ and εHf(t) values and the Hf model ages of zircons from the Late Triassic Xiuwacu and Hongshan intrusive rocks in the southern Yidun Terrane.

5.3. Zircon Hf isotopes

Lu-Hf isotopic analyses were conducted on the same zircon grains as the O isotope analyses. The results are given in Appendix 3. The $\varepsilon_{Hf}(t)$ values of zircons from the phase 1, phase 2, MMEs, and Hongshan intrusions were back-calculated to 220, 217, 214, and 216 Ma, respectively. The $\varepsilon_{Hf}(t)^*$ values of zircons with inherited cores from the MMEs were back-calculated to the ages of each core. Fifteen analyses of the zircons from the phase 1 intrusion yielded $\varepsilon_{Hf}(t)$ values of 1.3 to 3.9 with T_{DM2} model ages of 1.00 to 1.17 Ga (Fig. 5). Fifteen analyses of the zircons from the phase 2 intrusion yielded $\varepsilon_{Hf}(t)$ values between −0.1 and 2.0 with T_{DM2} model ages of 1.13 to 1.26 Ga (Fig. 5). Nineteen analyses were conducted on the MME zircons. These Late Triassic zircons yielded $\varepsilon_{Hf}(t)$ values of 0.4 to 5.3 with T_{DM2} model ages of 0.91 to 1.23 Ga (Fig. 5). The cores of the inherited zircons yielded $\varepsilon_{Hf}(t)$ values of −26.9 to −1.1 with T_{DM2} model ages of 1.17 to 2.32 Ga. Fifteen analyses of the Hongshan zircons yielded $\varepsilon_{Hf}(t)$ values of 0.6 to 3.9 with T_{DM2} model ages of 1.00 to 1.21 Ga (Fig. 5).

5.4. Major and trace elements

Major and trace elemental data for the Late Triassic Xiuwacu and Hongshan intrusive rocks are listed in Appendix 4. The Xiuwacu MMEs are metaluminous (A/CNK = 0.92–0.94 and A/NK 1.55–1.59) quartz monzonites (Fig. 6). They have relatively low SiO_2 contents (62.1–63.17 wt%) and relatively high Fe_2O_3 (4.47–5.06 wt%), MgO (2.03–2.09 wt%), CaO (4.08–4.29 wt%), and $Na_2O + K_2O$ (7.81–7.98 wt%) contents (Fig. 7). The Xiuwacu phase 1 intrusive rocks have variable and relatively high SiO_2 contents (63.4–70.5 wt %) and relatively low Fe_2O_3 (2.31–3.79 wt%), MgO (1.06–2.27 wt%), CaO (2.16–4.34 wt%), and $Na_2O + K_2O$ (7.37–8.57 wt%) contents (Fig. 7). Their A/CNK (0.89–1.02) and A/NK (1.36–1.56) values suggest they are metaluminous to slightly peraluminous quartz monzonites–granites (Fig. 6). The Xiuwacu phase 2 intrusive rocks have intermediate contents of SiO_2 (65.2–67.1 wt%), Fe_2O_3 (3.34–4.38 wt%), MgO (1.60–2.07 wt%), CaO (2.42–3.19 wt%), and $Na_2O + K_2O$ (6.87–7.42 wt%) (Fig. 7). Their A/CNK (0.99–1.10) and A/NK (1.54–1.62) values suggest they are peraluminous quartz monzonites (Fig. 6). The Hongshan intrusive rocks have the lowest contents of SiO_2 (59.6–61.8 wt%) and relatively high contents of Fe_2O_3 (5.51–6.35 wt%), MgO (2.37–2.72 wt%), CaO (3.30–4.18 wt%), and $Na_2O + K_2O$ (8.03–8.66 wt%) (Fig. 7). Their A/CNK (0.79–0.85) and A/NK (1.24–1.33) values suggest they are metaluminous monzonites–quartz monzonites (Fig. 6). The total alkali versus silica (TAS) diagram shows that the Xiuwacu MMEs and the phase 1 and 2 intrusive rocks are sub-alkaline, while the Hongshan intrusive rocks are alkaline (Fig. 6).

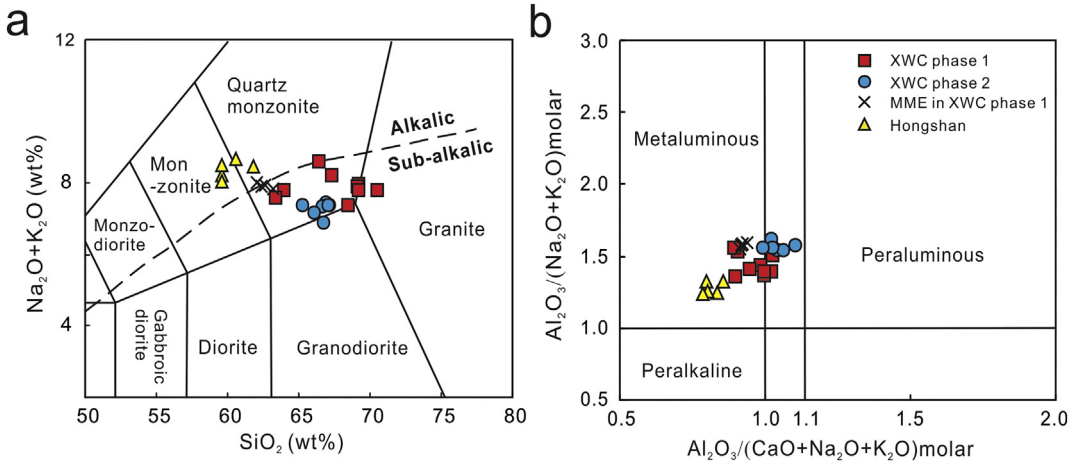

Fig. 6. (a) Total alkali versus SiO_2 diagram (Middlemost, 1994) and (b) A/NK versus A/CNK diagram (Maniar and Piccoli, 1989) for the Late Triassic Xiuwacu and Hongshan intrusive rocks in the southern Yidun Terrane.

On the chondrite-normalized rare earth element (REE) diagrams (Fig. 8), the samples from the two-phase intrusions of the Xiuwacu pluton display relatively highly fractionated REE patterns with La/Yb ratios of 18–35 and slightly negative Eu anomalies ($Eu/Eu^* = 0.56–0.87$) (Fig. 8). On the primitive mantle-normalized trace element diagrams, all the samples are depleted in Ba, Nb, Ta, P, and Ti and enriched in Rb, Th, and U (Fig. 8). The MMEs have relatively low Sr/Y (25.6–41.7), La/Yb (18.3–33.0), and Dy/Yb (1.53–1.78) ratios and very low Cr (6.83–8.12 ppm) and Ni (4.80–5.32 ppm) contents. The phase 1 intrusive rocks have variable intermediate Sr/Y (27.4–44.8), La/Yb (21.8–29.5), and Dy/Yb (1.53–1.88) ratios and Cr (8.39–16.4 ppm) and Ni (4.15–9.49 ppm) contents. The phase 2 intrusive rocks have high Sr/Y (43.7–57.0), La/Yb (23.3–34.7), and Dy/Yb (1.46–1.66) ratios and Cr (22.1–38.3 ppm) and Ni (13.4–28.1 ppm) contents. The Hongshan intrusive rocks have similar fractionated light REEs (LREEs)/heavy REEs (HREEs) with high La/Yb ratios (29–31) and rare Eu anomalies ($Eu/Eu^* = 0.95–1.00$) (Fig. 8). The Hongshan intrusive rocks are depleted in Th, Nb, Ta, and Ti and enriched in Ba, Th, and U. The

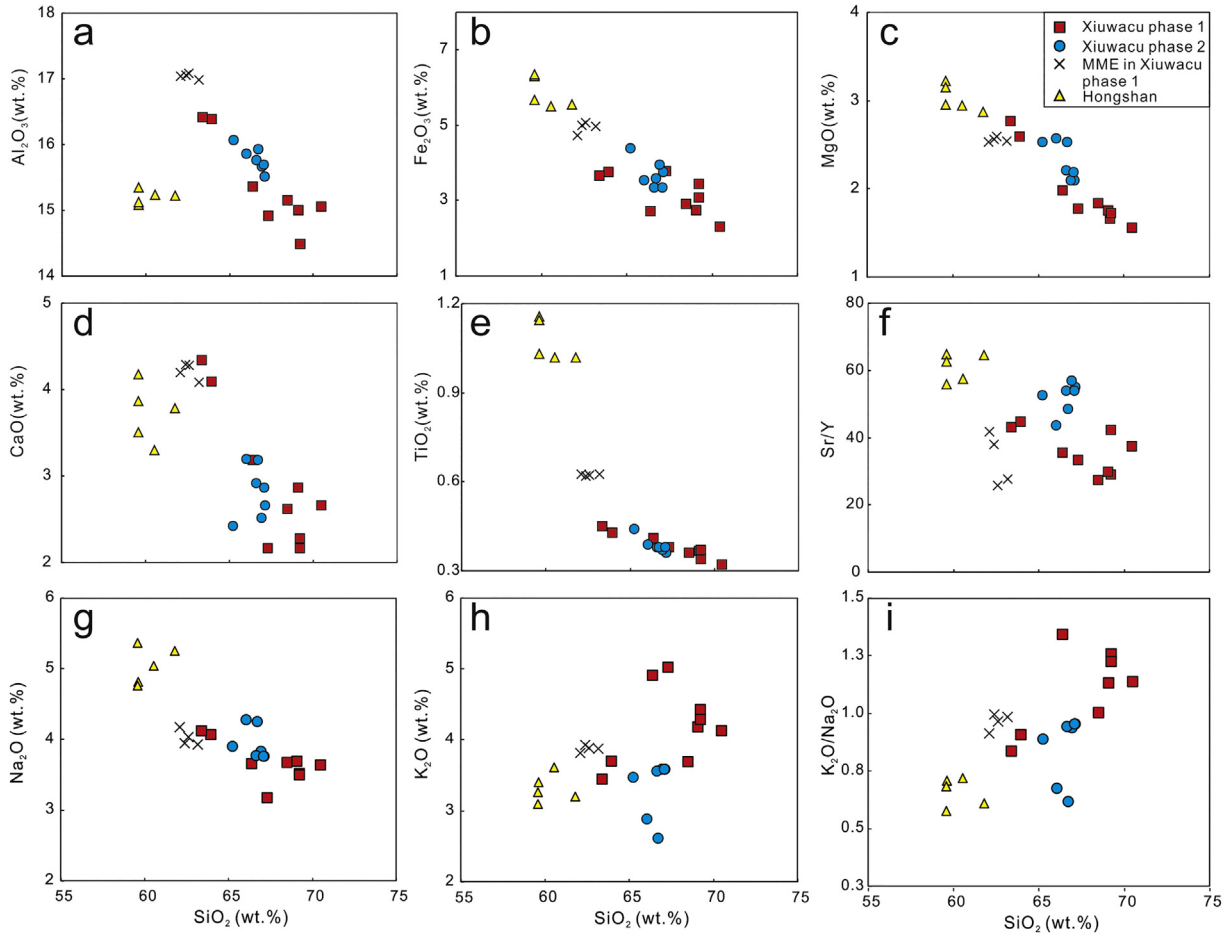

Fig. 7. Chemical variation diagrams for the Late Triassic Xiuwacu and Hongshan intrusive rocks in the southern Yidun Terrane.

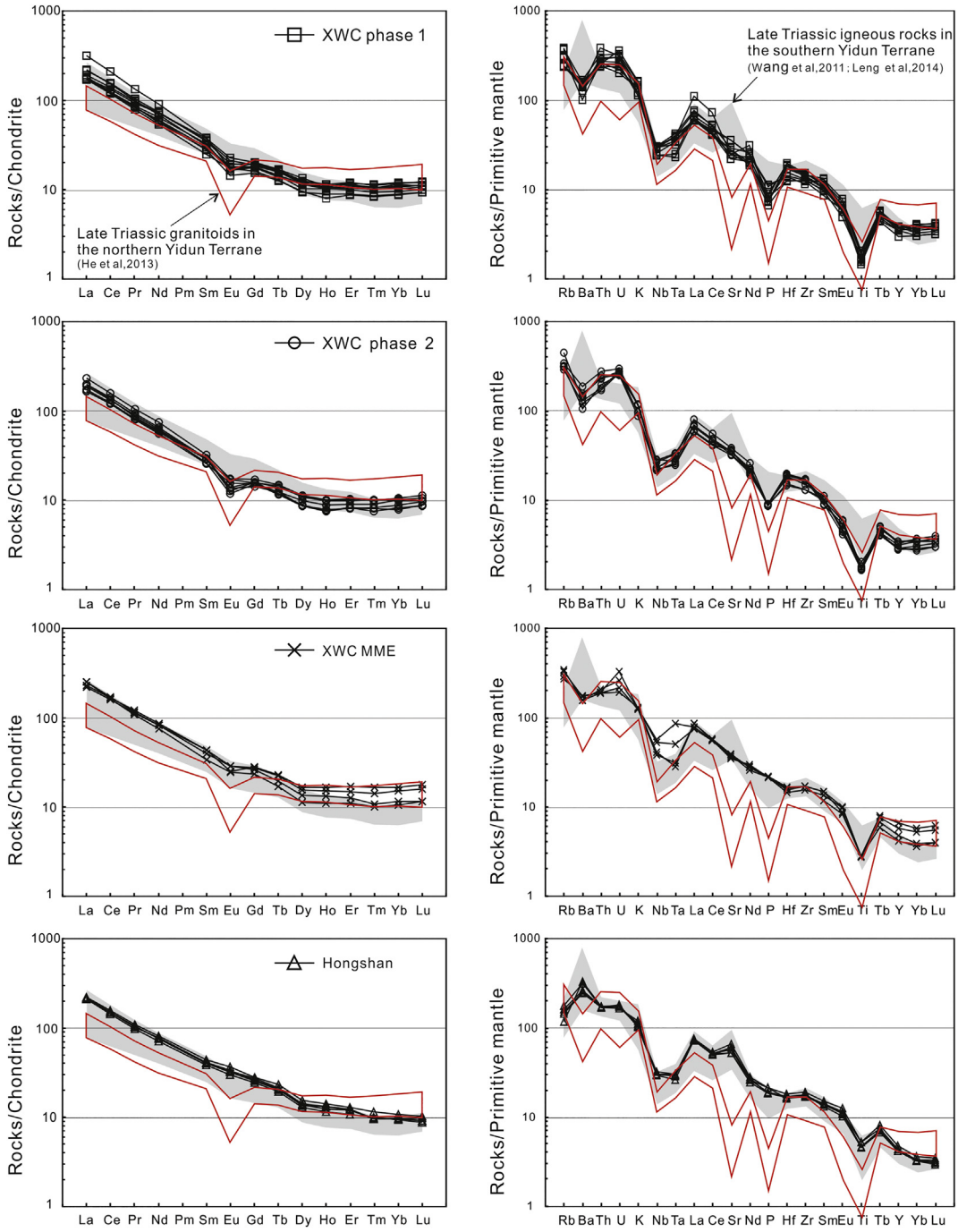

Fig. 8. Chondrite-normalized rare earth element (REE) and primitive mantle-normalized trace element diagrams for the Late Triassic intrusive rocks in the southern Yidun Terrane. Chondrite normalization values and primitive mantle values are from Sun and McDonough (1989). Data for the Late Triassic granitoids in the northern Yidun Terrane are from He et al. (2013) and those for the Late Triassic igneous rocks in the southern Yidun Terrane are from Wang et al. (2011) and Leng et al. (2014).

Hongshan intrusive rocks have relatively high Sr/Y (55.7–64.7), La/Yb (28.7–31.1), and Dy/Yb (2.07–2.19) ratios and low Cr (11.3–12.6 ppm) and Ni (7.31–8.43 ppm) contents.

5.5. Whole-rock Sr and Nd isotopes

The Sr and Nd isotopic compositions of the Xiuwacu and Hongshan intrusive rocks are presented in Appendix 5. The samples from the phase 1 intrusion (seven samples) exhibit homogeneous $(^{87}Sr/^{86}Sr)_i$ (0.7043–0.7053) and $\varepsilon_{Nd}(t)$ values (−2.2 to −0.8) with T_{DM2} = 1.05–1.15 Ga. The samples from the phase 2 intrusion (three samples) have similar values of $(^{87}Sr/^{86}Sr)_i$ (0.7043–0.7050) and $\varepsilon_{Nd}(t)$ (−1.2 to −1.6) with T_{DM2} = 1.10–1.13 Ga. The MMEs (three samples) exhibit $(^{87}Sr/^{86}Sr)_i$ = 0.7049–0.7064 and $\varepsilon_{Nd}(t)$ = −3.1 to −3.3 with T_{DM2} = 1.24–1.26 Ga. The Hongshan intrusive rocks (three samples) have $(^{87}Sr/^{86}Sr)_i$ = 0.7054–0.7056, $\varepsilon_{Nd}(t)$ = −2.8 to −1.3, and T_{DM2} = 1.10–1.14 Ga.

5.6. Zircon trace elements, magma oxygen fugacities, and crystallization temperatures

The zircon trace elements, magma oxygen fugacities, and crystallization temperatures of the Xiuwacu and Hongshan intrusive rocks are listed in Appendix 6. On the chondrite-normalized diagram, the zircons

are HREE enriched and LREE depleted with positive Ce anomalies and negative Eu anomalies. The titanium contents of the zircons in the Hongshan intrusive rocks (HS11-114, 7.0–14.5 ppm) are much higher than those of the zircons from the Xiuwacu intrusive rocks (phase1-XS12-17, 1.8–5.3 ppm; and phase2-XS12-07, 1.6–14.0 ppm). The titanium-in-zircon temperatures of the Hongshan intrusive rocks (HS11-114) are 749–818 °C, those of the Xiuwacu phase 1 intrusive rocks 636–726 °C, and those of the Xiuwacu phase 2 intrusive rocks 636–814 °C. The magma oxygen fugacities ($\log fO_2$) of the Hongshan intrusions (HS11-114) range from −11.3 to −6.4, those of the Xiuwacu phase 1 intrusion from −20.6 to −13.8, and those of the Xiuwacu phase 2 intrusion from −12.5 to −6.0.

6. Discussion

6.1. Petrogenesis of the Late Triassic intrusions of the southern Yidun Terrane

6.1.1. Petrogenesis of the MMEs in the Late Triassic Xiuwacu phase 1 intrusion

Several petrogenetic models have been proposed for the origin of MMEs, including (1) restites (Chen and Williams, 1990), (2) cognate fragments of cumulates (Dodge and Kistler, 1990; Shellnutt et al., 2010), (3) quenched mafic melts derived from the mantle (Eichelberger, 1980), and (4) mixing of mafic and felsic magmas (Barbarin and Didier, 1992; Chappell, 1996; Dorais et al., 1990; Farner et al., 2014; Liu et al., 2013; Plail et al., 2018; Van Der Laan and Wyllie, 1993; Wang et al., 2014b; Yang et al., 2007). In this study, the term mixing refers to that the complete combination of two components which, however, could potentially be chemically and isotopically discriminated (Chappell, 1996).

The MMEs in the Late Triassic Xiuwacu phase 1 intrusion have granitic textures with euhedral biotite and plagioclase, anhedral amphibole, and poikilitic textures with euhedral biotite enclosed in plagioclase (Fig. 2h–k). This indicates that the MMEs crystallized from a melt. The MMEs are quartz monazites with slightly high silica contents of 62.09–63.17 wt%. The Late Triassic zircons from MME sample XWC11-42 have variable and positive values of εHf(t) (+0.4 to +5.3), which indicate a mantle component in their source (Kemp et al., 2007). Due to the fact that their Hf isotope contents are much lower than those of MORBs (Mid-Ocean Ridge Basalts) and young oceanic-crust-derived melts (Fig. 9), it is likely that the MMEs were derived from a slightly enriched mantle source rather than slab melts. The negative εNd(t) values (−3.3 to −3.1) and low $(^{87}Sr/^{86}Sr)_i$ values (0.7049–0.7064) also support this suggestion, and indicate an EM-1 source (Fig. 10b). Such an EM-1 source would rule out the restitic origin model, as restites are dominated by metasedimentary components.

A small recrystallized felsic microgranular enclave (FME) made up of biotite, quartz, plagioclase, and K-feldspar was discovered within an MME (Fig. 2i–k). The recrystallized texture is characterized by a preferred orientation of biotite and 120° angles at the boundaries between the other mineral grains (Fig. 2k). As the texture of the FME is distinctly different from that of the MMEs, we conclude that the FME crystallized from a felsic melt. The SIMS U-Pb dating of the zircons from MME sample XWC11-42 show that many of the euhedral zircons in the MME have inherited cores that were rounded by sedimentary processes. Dating of these inherited zircons revealed five age peaks at 428–492, 534–643, ~817, ~1237, and ~1858 Ma (Fig. 4c; Appendix 1), which is consistent with the results of previous studies on the detrital and inherited zircons of the southern Yidun Terrane (Wang et al., 2013a). This indicates that a melt derived from metasedimentary rocks was involved in the source of the MMEs, and this contradicts the idea of the MMEs being cognate fragments of cumulates and quenched mafic melts. In addition, the MMEs have very similar mineral compositions, trace elemental patterns, and isotopic compositions relative to their host phase 1 intrusive rocks.

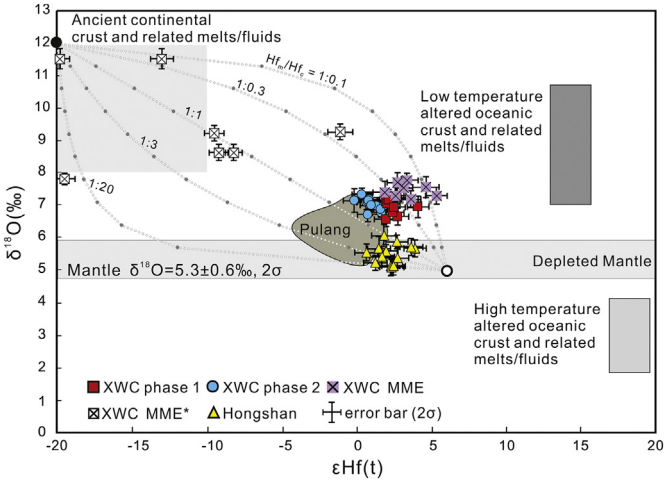

Fig. 9. $\delta^{18}O$ versus εHf(t) diagrams for the Late Triassic Xiuwacu and Hongshan intrusive rocks in the southern Yidun Terrane showing that the intrusions in the southern Yidun Terrane were predominantly derived from mantle-derived melts (70–100 wt%) that assimilated or mixed with melts derived from continental crust (0–30 wt%). The depleted mantle field is from Valley et al. (2005), the data for ancient continental crust, low-temperature altered oceanic crust, and high-temperature altered oceanic crust and related melts/fluids are from Zhu et al. (2017), and the data for the Pulang intrusive rocks are form Leng et al. (2018). The solid circle represents the end-member composition of melts/fluids derived from ancient continental crust ($\delta^{18}O$ = 5‰ and εHf (t) = 6), and the open circle represents the end-member composition of mantle-derived melts/fluids ($\delta^{18}O$ = 20‰ and εHf(t) = 12). The values of the two end-members are from the most enriched and most depleted oxygen and hafnium isotope compositions of this study. Hf_m/Hf_c represents the ratio of the hafnium contents of the mantle and crust. The dotted line represents assimilation or mixing between the two end-members. The symbols for the Xiuwacu MMEs and MMEs* on the diagram represent zircons from MMEs with Late Triassic ages and ancient cores, respectively. The zircon εHf(t) values for both MME and MME* were back-calculated to 214 Ma.

This also does not support the cumulates and quenched mafic melts models.

Moreover, the euhedral magmatic zircons with clear igneous oscillatory or planar growth zones have ages of 213.9 ± 1.7 Ma (Fig. 4d). The O and Hf isotope analyses of the Late Triassic zircons from the MMEs revealed variable $\delta^{18}O$ (4.80‰ to 7.79‰) and εHf(t) (+0.4 to +5.3) values. The zircons with ancient cores have more variable and higher $\delta^{18}O$ (7.83‰ to 11.5‰) and negative εHf(t) (−26.9 to −1.1) values (Fig. 9). All of this evidence strongly suggests a mixed source for the MMEs that was made up of an EM-1-derived basaltic melt and a felsic melt that was derived from metasedimentary rocks (Fig. 9, Fig. 10).

6.1.2. Petrogenesis of the Late Triassic Xiuwacu phase 1 intrusive rocks

The Xiuwacu phase 1 intrusive rocks have mineral components and zircon Hf-O and bulk-rock Sr-Nd isotopic compositions that are similar to those of the MMEs hosted by the phase 1 intrusion. The phase 1 intrusive rocks have a narrow range of zircon εHf(t) values (+1.3 to +3.9) and oxygen isotopic compositions ($\delta^{18}O$ = 6.58‰ to 7.31‰), which fall within the ranges of the values for the MMEs (εHf(t) = +0.4 to +5.3 and $\delta^{18}O$ = 4.80‰ to 7.79‰). This indicates that the Xiuwacu phase 1 intrusive rocks were also formed by the mixing of EM-1 melts and felsic melts, but they are more homogeneous than the MMEs (Figs. 9, 10). On the other hand, their εNd(t) (−2.2 to −0.8) and $(^{87}Sr/^{86}Sr)_i$ (0.7043–0.7053) values are similar but slightly more depleted than those of the MMEs (Fig. 10a). This indicates that the whole-rock Sr-Nd isotopes of the MMEs contain relatively more felsic components, and this is consistent with the fact that the MMEs contain small FMEs and inherited zircons. The information provided by the in situ zircon Hf-O isotope and bulk-rock Sr-Nd isotope analyses confirms that the isotopic compositions of the zircons can provide information on the magma source. Whole rock geochemistry can only reveal information about the mixture, rather than the end-members, but in situ zircon

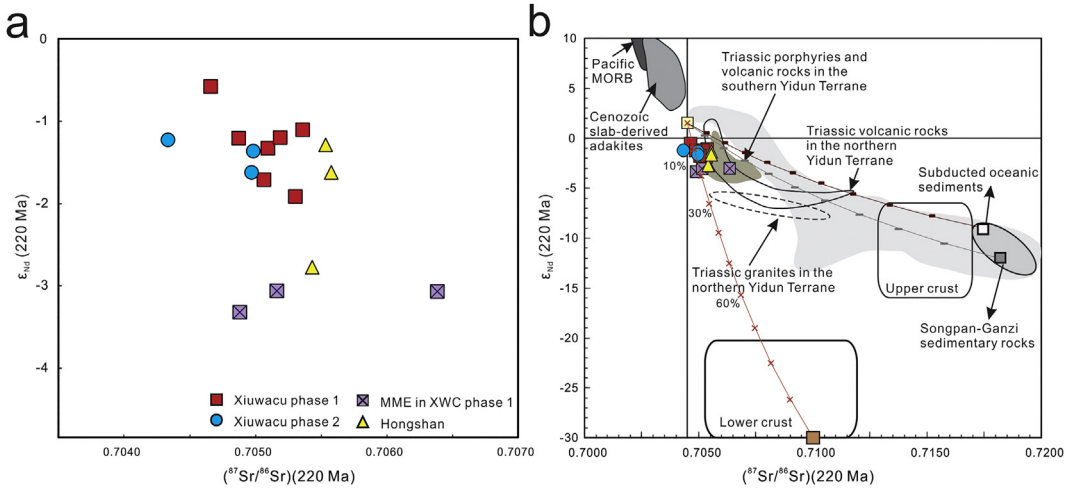

Fig. 10. $\varepsilon_{Nd}(t)$ versus $(^{87}Sr/^{86}Sr)_i$ diagram for the Xiuwacu and Hongshan intrusive rocks. The lower and upper continental crust fields are from Jahn et al. (1999), the Cenozoic slab-derived adakites are from Wang et al. (2011), the Late Triassic arc magmas in the southern Yidun Terrane are from Leng et al. (2014) and Wang et al. (2011), the Late Triassic granites and volcanic rocks in the northern Yidun Terrane are from He et al. (2013) and Wang et al. (2014b), the Songpan–Ganzi sedimentary rocks are from Wu et al. (2010), and the global subducted oceanic sediments are from Plank and Langmuir (1998). The different colored squares connected by solid lines represent the different end-members of the Late Triassic basalts from the southern Yidun Terrane (yellow: Sr = 600 ppm, Nd = 30 ppm, $\varepsilon_{Nd}(t) = 1.5$, and $(^{87}Sr/^{86}Sr)_i = 0.7045$); lower continental crust (brown: Sr = 300 ppm, Nd = 24 ppm, $\varepsilon_{Nd}(t) = -30$, and $(^{87}Sr/^{86}Sr)_i = 0.7100$; Jahn et al., 1999); global average subducted oceanic sediments (white: Sr = 327 ppm, Nd = 27 ppm, $\varepsilon_{Nd}(t) = -8.93$, and $(^{87}Sr/^{86}Sr)_i = 0.7173$; Plank and Langmuir, 1998); and average value of Songpan–Ganzi sedimentary rocks (gray: Sr = 320, Nd = 27 ppm, $\varepsilon_{Nd}(t) = -12$, and $(^{87}Sr/^{86}Sr)_i = 0.7181$; Wu et al., 2010).

Hf-O isotopes can record the mixing process in their heterogeneous values (Figs. 9, 10).

The Late Triassic Xiuwacu phase 1 intrusive rocks are quartz monzonites–granites with silica contents ranging from 63.37 to 70.46 wt%. The lowest of these silica contents is slightly higher than the silica contents of the MMEs (SiO_2 = 62.09–63.17 wt%), even though the MMEs incorporated quite a lot of felsic end-member material during mixing. This indicates that the direct mixing of mantle-derived basaltic magmas and felsic melts did not in this case generate melts as felsic as the phase 1 intrusive rocks. This conclusion is supported by the results of previous studies that showed the MMEs are always andesitic and have lower silica contents than their host rocks which are always dioritic–granitic with a mixture of isotopic compositions (Barbarin and Didier, 1992; Dorais et al., 1990; Farner et al., 2014; Liu et al., 2013; Plail et al., 2018; Wang et al., 2014b; Yang et al., 2007). On this basis, we infer that the direct mixing of basaltic and felsic melts would commonly generate andesitic melts, and that an additional crystal fractionation process is required to raise the silica content of many of the observed magmas. This is probably because the mixing could only occur in a basalt-dominated magma chamber where the temperatures were high and viscosities low (Farner et al., 2014).

In addition, the phase 1 intrusive rocks that host the MMEs have zircons with more homogeneous Hf-O isotopic compositions than those in the MMEs. This indicates that the phase 1 intrusion were generated from a homogeneous source rather than from a heterogeneous melt such as that which generated the MMEs. The MMEs most likely represent a later injection of mixture between mafic and felsic melts into the magma chamber of the phase 1 intrusion. Nevertheless, the earlier-formed phase 1 intrusion were derived from a homogeneous source that had already undergone mixing.

It is likely that the magmas of the phase 1 intrusion were formed in a MASH zone within the lower crust where it was hot enough to form a homogeneous mixed melt (Farner et al., 2014; Lee and Bachmann, 2014). The basaltic melts were derived from the partial melting of the metasomatized mantle wedge that was underplating the lower crust, and these melts were then mixed with or assimilated lower crustal melts. These mixed melts subsequently underwent fractional crystallization within the lower crust to generate the andesitic–dioritic magmas. With increasing buoyancy, the relatively homogenous andesitic–dioritic magmas entered an upper crustal magma chamber and underwent further crystal fractionation to generate the phase 1 intrusive rocks. Moreover, as the phase 1 intrusive rocks in the Xiuwacu region have homogenous isotopic compositions and no mafic cumulates, we infer that the crystal fractionation occurred mainly in the MASH zone and during ascent. The variable and low Fe, Mg, Ca, Cr, and Ni contents (Fig. 7) suggest fractionation of Fe–Mg-bearing minerals such as olivine and clinopyroxene. The relatively high Sr/Y, La/Yb, and Rb/Sr ratios, the low Ba/Rb ratios, the low contents of Ba and Sr, and the negative Eu anomalies of the phase 1 intrusive rocks (Figs. 7, 8, 11a–b), as well as the fractionation modeling results (Fig. 11c), suggest that amphibole, plagioclase, and biotite fractionation occurred in the magma chamber.

6.1.3. Petrogenesis of the Late Triassic Xiuwacu phase 2 intrusive rocks

Generally, the Xiuwacu phase 2 intrusive rocks have whole-rock major and trace element, Sr-Nd isotope, and zircon Hf-O isotope compositions that are similar to those of the phase 1 intrusive rocks (Figs. 6, 7, 8, 9, 10). This indicates that the phase 1 and 2 intrusions had similar sources. However, the phase 2 intrusive rocks have higher Cr (22.1–38.3 ppm) and Ni (13.4–28.1 ppm) contents (Fig. 12) and higher Na_2O/K_2O (1.1–1.6), A/CNK (0.99–1.10), Sr/Y (43.7–57.0), and La/Yb (23.3–34.7) ratios than the phase 1 intrusive rocks (Cr = 8.39–16.4 ppm, Ni = 4.15–9.49 ppm, Na_2O/K_2O = 0.6–1.2, A/CNK = 0.89–1.02, Sr/Y = 27.4–44.8, and La/Yb = 21.8–29.5). However, the phase 1 and 2 intrusive rocks have similar SiO_2 contents.

Higher or lower degrees of fractional crystallization of the parental magma of the phase 1 intrusive rocks cannot explain these differences. Higher degrees of fractional crystallization of mafic minerals would have decreased the Cr and Ni contents because Cr and Ni are compatible elements and are incorporated in Fe–Mg-bearing minerals (Chiaradia et al., 2011). Higher degrees of plagioclase fractionation would have decreased the Na_2O/K_2O, Sr/Y, and La/Yb ratios. Lower degrees of fractionation would have generated a melt with lower SiO_2 contents than the phase 1 intrusive rocks, which is incompatible with the geochemistry described above.

The compositional differences between the two phases of intrusive rock could not have been caused by the injection of new mafic magma into the phase 2 magma because the phase 2 intrusive rocks have slightly higher values of $\delta^{18}O$ (6.73‰ to 7.41‰) and lower values of $\varepsilon Hf(t)$ (−1 to +2) than the phase 1 intrusive rocks ($\varepsilon Hf(t)$ = +1.3 to +3.9 and $\delta^{18}O$ = 6.58‰ to 7.31‰; Figs. 5, 9). This indicates that the phase 2 intrusion involved the incorporation of slightly more continental crustal material (Kemp et al., 2007). Moreover, the phase 2 magmas

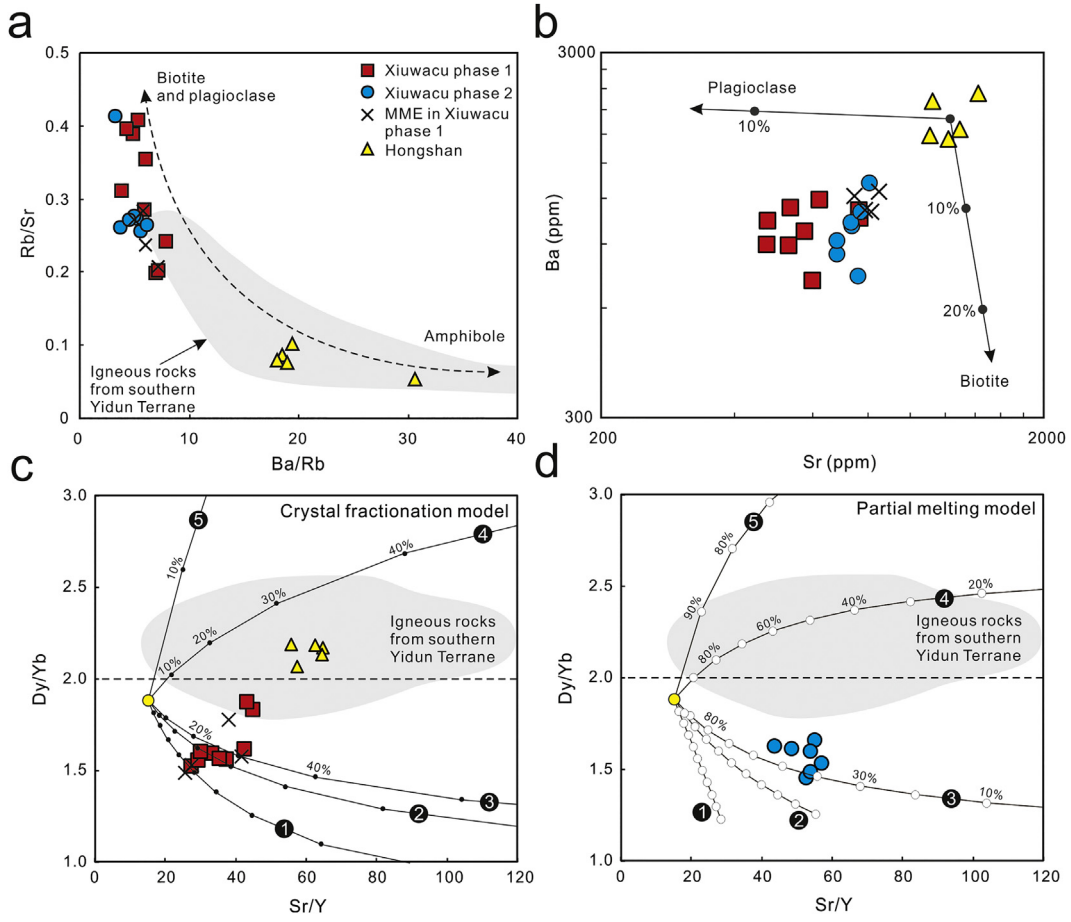

Fig. 11. (a) Rb/Sr versus Ba/Rb diagram, (b) Ba versus Sr diagram, (c) Dy/Yb versus Sr/Y diagram for the crystallization of basaltic melts, and (d) partial melting of basaltic lower crust for the Late Triassic Xiuwacu and Hongshan intrusions in the southern Yidun Terrane. The dashed line with arrowheads in plot (a) illustrates that biotite and plagioclase crystallization or residue during the crystal fractionation or partial melting process led to melts with high Rb/Sr and low Ba/Rb ratios, while amphibole would have caused the opposite trend. (b) Vectors for plagioclase and biotite fractionation ($C_l = C_o \cdot (1 - F)^{(D-1)}$) calculated using partition coefficents from Ewart and Griffin (1994). Tick marks indicate the percentage of the mineral phase removed, in 10% intervals. The solid curves with small circles in plots (c) and (d) represent different degrees of crystal fractionation ($C_l = C_o \cdot (1 - F)^{(D-1)}$) and partial melting ($C_l = C_o/[F + D(1 - F)]$), respectively. The percentage values on these curves represent the weight percent of melt in these models. The numbers in the black solid circles in plots (c) and (d) represent the residual minerals in the model: 1 = 60% amphibole and 40% plagioclase; 2 = 80% amphibole and 20% plagioclase; 3 = 95% amphibole and 5% garnet; 4 = 85% amphibole and 15% garnet; and 5 = 20% amphibole, 30% garnet, and 50% clinopyroxene. The initial Dy, Yb, Sr, and Y contents of the basaltic melts and basaltic crust are 4.1 ppm, 2.2 ppm, 300 ppm, and 20 ppm (Gao et al., 1999; Wang et al., 2013b). The partition coefficients of Dy, Yb, Sr, and Y for the basaltic melts and the minerals are from Sisson (1994) and Qian and Hermann (2013). The igneous rock field in the southern Yidun Terrane is from Leng et al. (2014) and Wang et al. (2011).

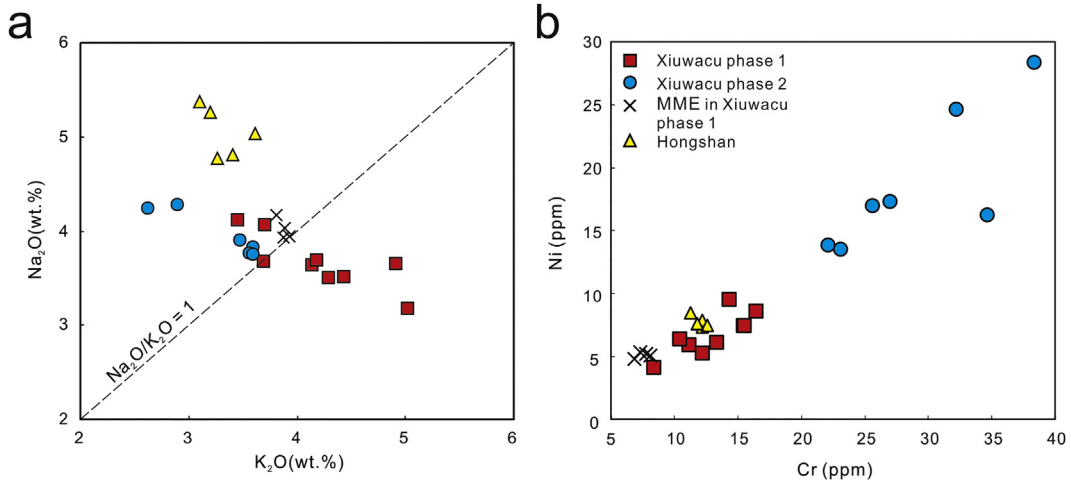

Fig. 12. (a) Na_2O versus K_2O diagram, and (b) Ni versus Cr diagram for the Late Triassic Xiuwacu and Hongshan intrusive rocks in the southern Yidun Terrane.

were more mobile, based on the porphyritic textures of the phase 2 rocks and their relatively fast cooling (Fig. 2c–e). The continental crustal material could not have been added to the phase 2 magmas in the upper crust, so it was probably incorporated in the lower crust.

The Ti-in-zircon geothermometry results and the oxidation states of the Xiuwacu intrusive rocks indicate that the oxygen fugacities and crystallization temperatures of the phase 2 magmas were slightly higher than those of the phase 1 magmas (Fig. 13). This suggests that the phase 2 magmas were derived from a source with higher oxygen fugacities and temperatures than the phase 1 magmas. It is more likely that the phase 2 magmas were generated by higher degrees of partial melting of the newly-underplated basaltic lower crust formed in the MASH zone, from where the phase 1 magmas had previously been derived. The newly-underplated basaltic lower crust was formed by sustained MASH processes involving a high degree of crustal contamination. In addition, higher degrees of partial melting of the newly-underplated basaltic lower crust would have generated melts with higher oxygen fugacities, higher Na_2O/K_2O ratios, and higher Ni and Cr contents (Atherton and Petford, 1993). Forty to 50% partial melting of this newly-underplated basaltic lower crust with residual minerals such as amphibole, plagioclase, and biotite could have generated the phase 2 magmas, based on the Rb/Sr versus Ba/Rb, Ba versus Sr, and Dy/Yb versus Sr/Y plots (Fig. 11).

6.1.4. Petrogenesis of the Late Triassic Hongshan intrusive rocks

The Late Triassic Hongshan intrusive rocks have low $\delta^{18}O$ values of 5.11‰ to 6.07‰ with a weighted mean value of 5.51 ± 0.1‰ (2σ) (Figs. 5, 9), which is within the range of mantle-derived magmas (5.3 ± 0.6‰, 2σ; Valley et al., 2005). This indicates that the Hongshan intrusive rocks were derived dominantly from a mantle source with little or no crustal contamination. Their relatively low $\varepsilon_{Hf}(t)$ values of 0.6 to 3.9, $(^{87}Sr/^{86}Sr)_i$ values of 0.7054–0.7056, and $\varepsilon_{Nd}(t)$ values of −2.8 to −1.3 (Figs. 9, 10) suggest that the Hongshan intrusive rocks were derived from an EM-1 source or from a newly-underplated basaltic lower crust formed by earlier MASH processes rather than from a depleted mantle source or a slab-derived melt (Fig. 9). However, their relatively high SiO_2 values (59.6–61.8 wt%) indicate that they could not have been derived solely and directly from the partial melting of mantle rocks (Laporte et al., 2014).

The Hongshan intrusive rocks have high $Fe_2O_3^T$ (5.51–6.35 wt%) and MgO (2.37–2.72 wt%) contents, very low Cr (11.3–12.6 ppm) and Ni (7.31–8.43 ppm) contents, and high Na_2O/K_2O (1.4–1.7) ratios (Fig. 12). This indicates that they were generated by the crystal fractionation of a mafic melt rather than by the partial melting of mafic rocks.

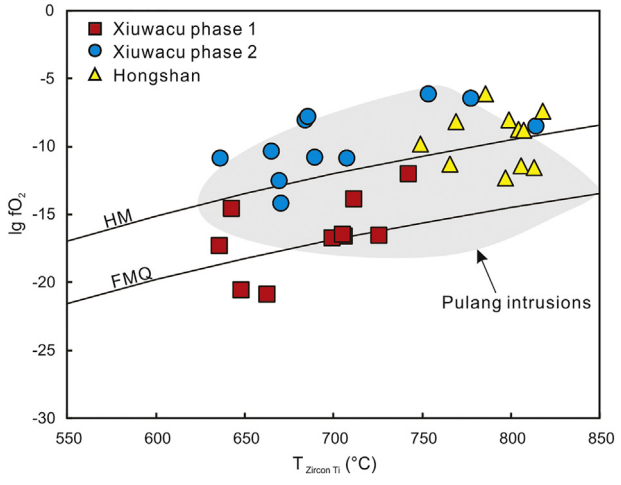

Fig. 13. Magma oxygen fugacity (fO_2) versus temperature ($T_{zircon\ Ti}$°C) diagram for the Late Triassic Xiuwacu and Hongshan intrusions in the southern Yidun Terrane. These data are listed in Appendix 6.

Because Cr and Ni are compatible in Fe- and Mg-bearing minerals, partial melting of a mafic rock would result in a melt with Cr and Ni contents >20 ppm, as in adakites (Chiaradia, 2009; Defant and Drummond, 1990). Although low degrees of partial melting of mafic rocks would have generated melts with low Cr and Ni contents, low degrees of partial melting would also have decreased the FeO and MgO contents and increased the SiO_2 content of the melt, resulting in a diorite or granite (Qian and Hermann, 2013). On the other hand, the sustained fractionation of olivine or clinopyroxene under high pressures would have decreased the Cr and Ni contents to very low values. This is seen in the case of the Hongshan intrusive rocks, even though they have relatively high FeO and MgO contents. The high $Na_2O + K_2O$ contents and the alkaline affinity (TAS diagram) of the Hongshan intrusive rocks also indicate that they were derived from the partial melting of an enriched mantle source that underwent fractionation with residual minerals such as pyroxene, olivine, and spinel. This process would have created a melt enriched in Na and K (Litvinovsky et al., 2015). In addition, the Hongshan intrusive rocks have high Dy/Yb (2.07–2.19), Sr/Y (55.7–64.7), and La/Yb (28.7–31.1) ratios and high Sr (1105–1421 ppm) and Ba (1742–2328 ppm) contents, which are probably the result of garnet and amphibole fractionation (Fig. 11). Therefore, all the evidence suggests that the Hongshan intrusive rocks were formed as a result of differentiation of a mantle-derived basaltic melt under high pressures.

6.2. Petrogenetic model for the Late Triassic andesitic and dioritic intrusive rocks in the southern Yidun Terrane

As discussed above, the MMEs in the Xiuwacu phase 1 intrusion were generated by the mixing of mantle-derived basaltic melts and felsic melts. The Xiuwacu phase 1 intrusive rocks were formed by high degrees of crystal fractionation of crustal-contaminated basaltic melts by a MASH process within the lower crust. The Xiuwacu phase 2 intrusive rocks were formed by high degrees of partial melting of the newly-underplated basaltic lower crust. The Hongshan intrusive rocks were formed by differentiation of mantle-derived basaltic magmas and high-pressure fractionation of olivine, pyroxene, garnet, and amphibole. As the Xiuwacu phase 2 and Hongshan intrusive rocks have the same age of ~216 Ma, and because they had higher temperatures and oxygen fugacities than the Xiuwacu phase 1 intrusive rocks, we infer that the Xiuwacu phase 2 and Hongshan intrusive activities were triggered by the same tectonic event. The increase in temperature was most likely triggered by the underplating of hot mafic mantle-derived melts.

As mentioned above, several researchers have shown that subduction-related magmatism in the Yidun Terrane occurred from 235 to 205 Ma. There were three main peaks of activity with earlier peaks at ~230 and ~225 Ma, and the latest peak at around 216 Ma (Cao et al., 2016; Hou et al., 2003; Hu et al., 2005; Kong et al., 2016; Leng et al., 2012; Leng et al., 2014; Leng et al., 2018; Li et al., 2011; Wang et al., 2011; Wang et al., 2013a; Wang et al., 2013b; Wang et al., 2018; Wu et al., 2017). A slab breakoff geodynamic model has been proposed to explain the tectonic and magma evolutionary processes (Wang et al., 2011; Wang et al., 2013a; Wang et al., 2013b; Wu et al., 2017). In the early stages from ~235 to ~220 Ma, the magmas were formed mainly as a result of the subduction of the Ganzi–Litang oceanic crust (Hou et al., 2003). It has been suggested that the late stage activity at ~216 Ma, as well as subsequent magmatism, was triggered by slab breakoff (Wang et al., 2011; Wang et al., 2013a; Wang et al., 2013b; Wu et al., 2017). Our new data show that the Xiuwacu phase 2 and Hongshan intrusions formed at ~216 Ma, indicating that the underplating of mantle-derived mafic melts under the Xiuwacu and Hongshan areas at this time was triggered by slab breakoff and the successive decompression and partial melting of the mantle wedge.

We propose, therefore, that during the early stage of subduction, the andesitic and dioritic intrusions in the southern Yidun Terrane were formed mainly as a result of the crystal fractionation of mantle-derived

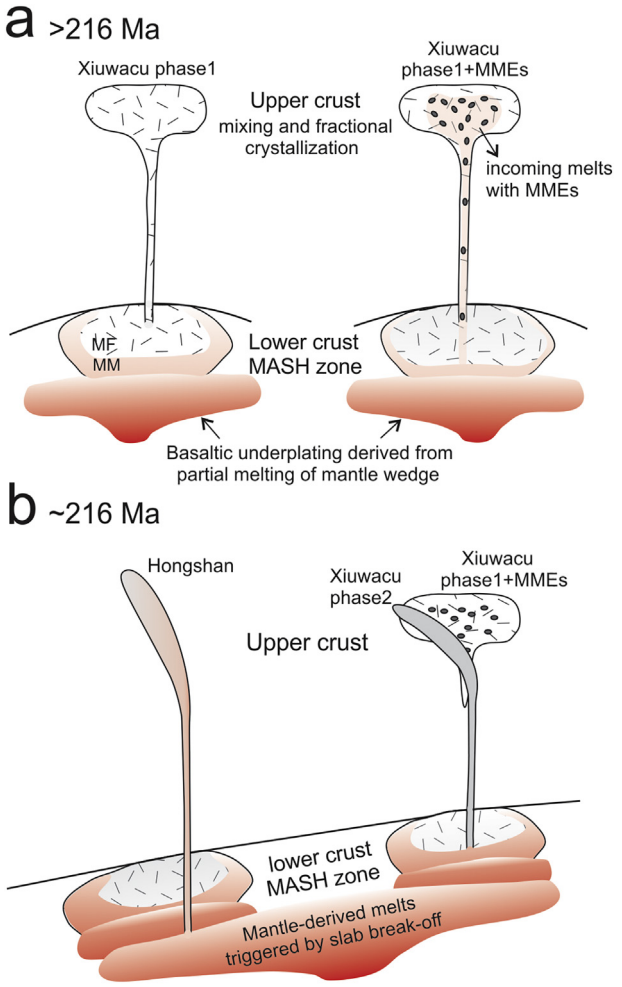

Fig. 14. Drawing showing the genesis of the Late Triassic Xiuwacu and Hongshan intrusive rocks. The left-hand side of diagram (a) shows that the Xiuwacu phase 1 intrusion were formed by crystal fractionation of melts derived from the MASH zone. MM = partial melting and mixing, MF = mixing and crystal fractionation. The right-hand side of the diagram (b) shows that the MMEs were formed later than the phase 1 intrusion by the mixing of mafic and felsic melts derived from the MASH zone. Partial melting of the mantle wedge forms basaltic magmas that underplate the lower crust and generate the MASH zone. Diagram (b) illustrates that at ~216 Ma, large amounts of mantle-derived melt triggered by slab breakoff, underplated the lower crust, creating heat and re-melting the earlier underplated basaltic lower crust and the MASH zone. The Hongshan intrusions were formed by the differentiation of mantle-derived basaltic melts at high pressures. The Xiuwacu phase 2 intrusion were derived by the partial melting of basaltic rocks from the earlier MASH zone.

basaltic magmas within the lower crust, but in combination with a certain amount of crustal contamination (Fig. 14a). On the other hand, during the later stage of slab breakoff, the andesitic and dioritic intrusions in the southern Yidun Terrane were formed by the partial melting of the newly-underplated basaltic lower crust and crystal fractionation of mantle-derived melts (Fig. 14b). Compared to previous researchers, we emphasize the importance of crystal fractionation of crustal-contaminated mantle-derived magmas in the genesis of the andesites and diorites. Partial melting of the newly underplated basaltic lower crust became significant during the slab breakoff process. Several researchers who have studied the magmas of recent arcs have suggested that the early stage of crystal fractionation causes the accumulation of Cu, and when these cumulates are re-melted during late-stage partial melting, they provide the metal for porphyry Cu mineralization (Chin et al., 2018; Lee et al., 2012). Therefore, partial melting of the newly underplated basaltic crust formed by early-stage MASH processes is probably an important prelude to porphyry copper mineralization. Such a model may help explain the genesis of andesitic–dioritic magmas and copper mineralization in other subduction zones where slab breakoff occurred.

7. Conclusions

(1) The Late Triassic Xiuwacu dioritic intrusions were produced in two phases of intrusive activity. Mafic microgranular enclaves (MMEs) are common in the phase 1 intrusion. The MMEs were formed by the mixing of basaltic melts and sedimentary-derived felsic melts. The phase 1 intrusive rocks were formed by the crystal fractionation of contaminated basaltic melts within the lower crust. The phase 2 intrusive rocks were generated by the partial melting of newly-underplated basaltic lower crust formed by early-stage MASH processes.

(2) The Hongshan intrusions were formed by the differentiation of mantle-derived basaltic melts at high pressures during slab breakoff.

(3) Based on our case study, we conclude that direct magma mixing of basaltic and felsic melts generated the andesitic MMEs. Crystal fractionation of mantle-derived basaltic magmas was critical to the genesis of the andesitic and dioritic magmas, but partial melting of newly-underplated basaltic lower crust during slab breakoff also became significant in the generation of these intrusions.

Acknowledgments

This study was supported financially by the strategic priority research program (B) of the Chinese Academy of Sciences (XDB18030000), the National Key R&D Program of China (2016YFC0600503), and the National Natural Science Foundation of China (41603052). We thank Prof. Qiu-Li Li, Mr. Guo-Qiang Tang, and Ms. Hong-Xia Ma for the SIMS U-Pb zircon dating and O isotope analyses, Prof. Zhao-Chu Hu for conducting the LA–(MC)–ICP–MS zircon Hf isotopic analyses, Dr. Zhi-Hui Dai for conducting the LA–ICP–MS zircon trace element analyses, Prof. Lian Zhou for the whole-rock Sr and Nd isotopic analyses, and Ms. Jing Hu for the major and trace element analyses.

Appendix. Supplementary data

Supplementary data to this article can be found online at https://doi.org/10.1016/j.lithos.2019.05.033.

References

Atherton, M.P., Petford, N., 1993. Generation of sodium-rich magmas from newly underplated basaltic crust. Nature 362, 144.
Barbarin, B., Didier, J., 1992. Genesis and evolution of mafic microgranular enclaves through various types of interaction between coexisting felsic and mafic magmas. Earth Environ. Sci. Trans. R. Soc. Edinb. 83 (1–2), 145–153.
Barnes, C.G., Frost, C.D., Nordgulen, O., Prestvik, T., 2012. Magma hybridization in the middle crust: possible consequences for deep-crustal magma mixing. Geosphere 8 (2), 518–533.
Cao, K., Xu, J.-F., Chen, J.-L., Huang, X.-X., Ren, J.-B., Zhao, X.-D., Liu, Z.-X., 2016. Double-layer structure of the crust beneath the Zhongdian arc, SW China: U–Pb geochronology and Hf isotope evidence. J. Asian Earth Sci. 115, 455–467.
Chang, C., 1997. Geology and Tectonics of Qinghai-Xizang Plateau Solid Earth Sciences Research in China. Science Press, Beijing, p. 153.
Chappell, B.W., 1996. Magma mixing and the production of compositional variation within granite suites: evidence from the granites of southeastern Australia. J. Petrol. 37 (3), 449–470.
Chen, Y.D., Williams, I.S., 1990. Zircon inheritance in mafic inclusions from Bega batholith granites, southeastern Australia: an ion microprobe study. J. Geophys. Res. Solid Earth 95 (B11), 17787–17796.
Chiaradia, M., 2009. Adakite-like magmas from fractional crystallization and melting-assimilation of mafic lower crust (Eocene Macuchi arc, Western Cordillera, Ecuador). Chem. Geol. 265 (3–4), 468–487.
Chiaradia, M., Muntener, O., Beate, B., 2011. Enriched basaltic andesites from mid-crustal fractional crystallization, recharge, and assimilation (Pilavo Volcano, Western Cordillera of Ecuador). J. Petrol. 52 (6), 1107–1141.

Chin, E.J., Shimizu, K., Bybee, G.M., Erdman, M.E., 2018. On the development of the calc-alkaline and tholeiitic magma series: a deep crustal cumulate perspective. Earth Planet. Sci. Lett. 482, 277–287.
Defant, M.J., Drummond, M.S., 1990. Derivation of some modern arc magmas by melting of young subducted lithosphere. Nature 347 (6294), 662–665.
Dodge, F.C.W., Kistler, R.W., 1990. Some additional observations on inclusions in the granitic rocks of the Sierra Nevada. J. Geophys. Res. Solid Earth 95 (B11), 17841–17848.
Dorais, M.J., Whitney, J.A., Roden, M.F., 1990. Origin of Mafic Enclaves in the Dinkey Creek Pluton, Central Sierra Nevada Batholith, California. J. Petrol. 31 (4), 853–881.
Eichelberger, J.C., 1980. Vesiculation of mafic magma during replenishment of silicic magma reservoirs. Nature 288 (5790), 446–450.
Ewart, A., Griffin, W.L., 1994. Application of proton-microprobe data to trace-element partitioning in volcanic rocks. Chem. Geol. 117 (1), 251–284.
Farner, M.J., Lee, C.-T.A., Putirka, K.D., 2014. Mafic–felsic magma mixing limited by reactive processes: a case study of biotite-rich rinds on mafic enclaves. Earth Planet. Sci. Lett. 393, 49–59.
Gao, S., Ling, W.L., Qiu, Y.M., Lian, Z., Hartmann, G., Simon, K., 1999. Contrasting geochemical and Sm-Nd isotopic compositions of Archean metasediments from the Kongling high-grade terrain of the Yangtze craton: evidence for cratonic evolution and redistribution of REE during crustal anatexis. Geochim. Cosmochim. Acta 63 (13–14), 2071–2088.
Hansen, J., Skjerlie, K.P., Pedersen, R.B., De la Rosa, J., 2002. Crustal melting in the lower parts of island arcs: an example from the Bremanger Granitoid complex, west Norwegian Caledonides. Contrib. Mineral. Petrol. 143 (3), 316–335.
He, D.F., Zhu, W.G., Zhong, H., Ren, T., Bai, Z.J., Fan, H.P., 2013. Zircon U–Pb geochronology and elemental and Sr–Nd–Hf isotopic geochemistry of the Daocheng granitic pluton from the Yidun Arc, SW China. J. Asian Earth Sci. 67-68, 1–17.
Hildreth, W., Moorbath, S., 1988. Crustal contributions to arc magmatism in the Andes of Central Chile. Contrib. Mineral. Petrol. 98 (4), 455–489.
Hou, Z.Q., Yang, Y.Q., Wang, H.P., Qu, X.M., Lv, Q.T., Huang, D.H., Wu, X.Z., Yu, J.J., Tang, S.H., Zhao, J.H., 2003. Collision-Orogenic Progress and Mineralization System of Yidun Arc. Geological Publishing House, Beijing (335 pp). (in Chinese).
Hu, J.M., Meng, Q.R., Shi, Y.R., Qu, H.J., 2005. SHRIMP U-Pb dating of zircons from granitoid bodies in the Songpan-Ganzi terrane and its implications. Acta Petrol. Sin. 21 (3), 867–880.
Hu, Z.C., Liu, Y.S., Gao, S., Liu, W.G., Zhang, W., Tong, X.R., Lin, L., Zong, K.Q., Li, M., Chen, H.H., 2012a. Improved in situ Hf isotope ratio analysis of zircon using newly designed X skimmer cone and jet sample cone in combination with the addition of nitrogen by laser ablation multiple collector ICP-MS. J. Anal. At. Spectrom. 27 (9), 1391–1399.
Hu, Z.C., Liu, Y.S., Gao, S., Xiao, S.Q., Zhao, L.S., Gunther, D., Li, M., Zhang, W., Zong, K.Q., 2012b. A "wire" signal smoothing device for laser ablation inductively coupled plasma mass spectrometry analysis. Spectrochim. Acta Part B-Atomic Spectrosc. 78, 50–57.
Jahn, B.M., Wu, F.Y., Lo, C.H., Tsai, C.H., 1999. Crust-mantle interaction induced by deep subduction of the continental crust: Geochemical and Sr-Nd isotopic evidence from post-collisional mafic-ultramafic intrusions of the northern Dabie complex, Central China. Chem. Geol. 157 (1–2), 119–146.
Kemp, A.I.S., Hawkesworth, C.J., Foster, G.L., Paterson, B.A., Woodhead, J.D., Hergt, J.M., Gray, C.M., Whitehouse, M.J., 2007. Magmatic and crustal differentiation history of granitic rocks from Hf-O isotopes in zircon. Science 315 (5814), 980–983.
Kong, D.-X., Xu, J.-F., Chen, J.-L., 2016. Oxygen isotope and trace element geochemistry of zircons from porphyry copper system: implications for late Triassic metallogenesis within the Yidun Terrane, southeastern Tibetan Plateau. Chem. Geol. 441, 148–161.
Laporte, D., Lambart, S., Schiano, P., Ottolini, L., 2014. Experimental derivation of nepheline syenite and phonolite liquids by partial melting of upper mantle peridotites. Earth Planet. Sci. Lett. 404, 319–331.
Lee, C.-T.A., Bachmann, O., 2014. How important is the role of crystal fractionation in making intermediate magmas? Insights from Zr and P systematics. Earth Planet. Sci. Lett. 393, 266–274.
Lee, C.T.A., Luffi, P., Chin, E.J., Bouchet, R., Dasgupta, R., Morton, D.M., Le Roux, V., Yin, Q.Z., Jin, D., 2012. Copper systematics in Arc magmas and implications for crust-mantle differentiation. Science 336 (6077), 64–68.
Leng, C.B., Zhang, X.C., Hu, R.Z., Wang, S.X., Zhong, H., Wang, W.Q., Bi, X.W., 2012. Zircon U–Pb and molybdenite Re–Os geochronology and Sr–Nd–Pb–Hf isotopic constraints on the genesis of the Xuejiping porphyry copper deposit in Zhongdian, Northwest Yunnan, China. J. Asian Earth Sci. 60 (0), 31–48.
Leng, C.B., Huang, Q.Y., Zhang, X.C., Wang, S.X., Zhong, H., Hu, R.Z., Bi, X.W., Zhu, J.J., Wang, X.S., 2014. Petrogenesis of the Late Triassic volcanic rocks in the Southern Yidun arc, SW China: constraints from the geochronology, geochemistry, and Sr–Nd–Pb–Hf isotopes. Lithos 190–191 (0), 363–382.
Leng, C.-B., Gao, J.-F., Chen, W.T., Zhang, X.-C., Tian, Z.-D., Guo, J.-H., 2018. Platinum-group elements, zircon Hf-O isotopes, and mineralogical constraints on magmatic evolution of the Pulang porphyry Cu-Au system, SW China. Gondwana Res. 62, 163–177.
Li, X.H., Li, W.X., Wang, X.C., Li, Q.L., Liu, Y., Tang, G.Q., 2009. Role of mantle-derived magma in genesis of early Yanshanian granites in the Nanling Range, South China: in situ zircon Hf-O isotopic constraints. Sci. China Ser. D 52 (9), 1262–1278.
Li, X.H., Long, W.G., Li, Q.L., Liu, Y., Zheng, Y.F., Yang, Y.H., Chamberlain, K.R., Wan, D.F., Guo, C.H., Wang, X.C., 2010. Penglai zircon megacrysts: a potential new working reference material for microbeam determination of Hf–O isotopes and U–Pb age. Geostand. Geoanal. Res. 34 (2), 117–134.
Li, W.C., Zeng, P.S., Hou, Z.Q., White, N.C., 2011. The pulang porphyry copper deposit and associated felsic intrusions in Yunnan Province, Southwest China. Econ. Geol. 106 (1), 79–92.
Litvinovsky, B.A., Jahn, B.M., Eyal, M., 2015. Mantle-derived sources of syenites from the A-type igneous suites - new approach to the provenance of alkaline silicic magmas. Lithos 232, 242–265.
Liu, Y.S., Hu, Z.C., Gao, S., Gunther, D., Xu, J., Gao, C.G., Chen, H.H., 2008. In situ analysis of major and trace elements of anhydrous minerals by LA-ICP-MS without applying an internal standard. Chem. Geol. 257 (1–2), 34–43.
Liu, Y.S., Gao, S., Hu, Z.C., Gao, C.G., Zong, K.Q., Wang, D.B., 2010. Continental and oceanic crust recycling-induced melt-peridotite interactions in the Trans-North China Orogen: U-Pb Dating, Hf isotopes and trace elements in zircons from mantle xenoliths. J. Petrol. 51 (1–2), 537–571.
Liu, L., Qiu, J.-S., Li, Z., 2013. Origin of mafic microgranular enclaves (MMEs) and their host quartz monzonites from the Muchen pluton in Zhejiang Province, Southeast China: implications for magma mixing and crust–mantle interaction. Lithos 160-161, 145–163.
Lu, Y.J., Kerrich, R., McCuaig, T.C., Li, Z.X., Hart, C.J.R., Cawood, P.A., Hou, Z.Q., Bagas, L., Cliff, J., Belousova, E.A., Tang, S.H., 2013. Geochemical, Sr-Nd-Pb, and zircon Hf-O isotopic compositions of eocene-oligocene shoshonitic and potassic adakite-like Felsic Intrusions in Western Yunnan, SW China: petrogenesis and tectonic implications. J. Petrol. 54 (7), 1309–1348.
Ludwig, K.R., 2003. ISOPLOT 3.00: A Geochronological Toolkit for Microsoft Excel. Berkeley Geochronology Center, California, Berkeley.
Maniar, P.D., Piccoli, P.M., 1989. Tectonic discrimination of granitoids. Bull. Geol. Soc. Am. 101 (5), 635.
Middlemost, E.A.K., 1994. Naming materials in the magma/igneous rock system. Earth-Sci. Rev. 37 (3–4), 215–224.
Pietranik, A., Slodczyk, E., Hawkesworth, C.J., Breitkreuz, C., Storey, C.D., Whitehouse, M., Milke, R., 2013. Heterogeneous zircon cargo in voluminous Late Paleozoic Rhyolites: Hf, O isotope and Zr/Hf records of plutonic to volcanic magma evolution. J. Petrol. 54 (8), 1483–1501.
Plail, M., Edmonds, M., Woods, A.W., Barclay, J., Humphreys, M.C.S., Herd, R.A., Christopher, T., 2018. Mafic enclaves record syn-eruptive basalt intrusion and mixing. Earth Planet. Sci. Lett. 484, 30–40.
Plank, T., Langmuir, C.H., 1998. The chemical composition of subducting sediment and its consequences for the crust and mantle. Chem. Geol. 145 (3–4), 325–394.
Qi, L., Hu, J., Gregoire, D.C., 2000. Determination of trace elements in granites by inductively coupled plasma mass spectrometry. Talanta 51 (3), 507–513.
Qian, Q., Hermann, J., 2013. Partial melting of lower crust at 10–15 kbar: constraints on adakite and TTG formation. Contrib. Mineral. Petrol. 165 (6), 1195–1224.
Qu, X.M., Hou, Z.Q., Tang, S.H., 2003. Age of intraplate volcanism in the back-arc area of Yidun island arc and its significance. Petrologica Et Mineralogica 22 (2), 131–137 (in Chinese with English abstract).
Reid, A., Wilson, C.J.L., Shun, L., Pearson, N., Belousova, E., 2007. Mesozoic plutons of the Yidun Arc, SW China: U/Pb geochronology and Hf isotopic signature. Ore Geol. Rev. 31 (1–4), 88–106.
Richards, J.P., 2003. Tectono-magmatic precursors for porphyry Cu-(Mo-Au) deposit formation. Econ. Geol. Bull. Soc. Econ. Geol. 98 (8), 1515–1533.
Shellnutt, J.G., Jahn, B.M., Dostal, J., 2010. Elemental and Sr–Nd isotope geochemistry of microgranular enclaves from peralkaline A-type granitic plutons of the Emeishan large igneous province, SW China. Lithos 119 (1), 34–46.
Sisson, T.W., 1994. Hornblende-melt trace-element partitioning measured by ion microprobe. Chem. Geol. 117 (1), 331–344.
Stern, R.J., 2002. Subduction zones. Rev. Geophys. 40 (4), 1012.
Sun, S.S., McDonough, W.F., 1989. Chemical and isotopic systematics of oceanic basalts: implications for mantle composition and processes. Geol. Soc. Lond. Spec. Publ. 42 (1), 313–345.
Trail, D., Bruce Watson, E., Tailby, N.D., 2012. Ce and Eu anomalies in zircon as proxies for the oxidation state of magmas. Geochim. Cosmochim. Acta 97, 70–87.
Valley, J.W., Lackey, J.S., Cavosie, A.J., Clechenko, C.C., Spicuzza, M.J., Basei, M.A.S., Bindeman, I.N., Ferreira, V.P., Sial, A.N., King, E.M., Peck, W.H., Sinha, A.K., Wei, C.S., 2005. 4.4 billion years of crustal maturation: oxygen isotope ratios of magmatic zircon. Contrib. Mineral. Petrol. 150 (6), 561–580.
Van Der Laan, S.R., Wyllie, P.J., 1993. Experimental Interaction of Granitic and Basaltic Magmas and Implications for Mafic Enclaves. J. Petrol. 34 (3), 491–517.
Wang, Q.W., Wang, K.M., Han, Z.Z., Fu, X.F., Liang, B., Yao, Z.D., Dai, Z.M., Luo, S.L., Zhong, C.H., Wei, Y.F., 2008. The Granite in West Sichuan and its Metallogenic Series. Geological Publishing House, Beijing (305 pp., in Chinese).
Wang, B.Q., Zhou, M.F., Li, J.W., Yan, D.P., 2011. Late Triassic porphyritic intrusions and associated volcanic rocks from the Shangri-La region, Yidun terrane, Eastern Tibetan Plateau: Adakitic magmatism and porphyry copper mineralization. Lithos 127 (1–2), 24–38.
Wang, B.Q., Wang, W., Chen, W.T., Gao, J.F., Zhao, X.F., Yan, D.P., Zhou, M.F., 2013a. Constraints of detrital zircon U–Pb ages and Hf isotopes on the provenance of the Triassic Yidun Group and tectonic evolution of the Yidun Terrane, Eastern Tibet. Sediment. Geol. 289 (0), 74–98.
Wang, B.Q., Zhou, M.F., Chen, W.T., Gao, J.F., Yan, D.P., 2013b. Petrogenesis and tectonic implications of the Triassic volcanic rocks in the northern Yidun Terrane, Eastern Tibet. Lithos 175-176, 285–301.
Wang, X.S., Bi, X.W., Leng, C.B., Zhong, H., Tang, H.F., Chen, Y.W., Yin, G.H., Huang, D.Z., Zhou, M.F., 2014a. Geochronology and geochemistry of Late Cretaceous igneous intrusions and Mo-Cu-(W) mineralization in the southern Yidun Arc, SW China: implications for metallogenesis and geodynamic setting. Ore Geol. Rev. 61, 73–95.
Wang, X.S., Hu, R.Z., Bi, X.W., Leng, C.B., Pan, L.C., Zhu, J.J., Chen, Y.W., 2014b. Petrogenesis of Late Cretaceous I-type granites in the southern Yidun Terrane: new constraints on the Late Mesozoic tectonic evolution of the eastern Tibetan Plateau. Lithos 208–209 (0), 202–219.
Wang, X.S., Bi, X.W., Hu, R.Z., Leng, C.B., Yu, H.J., Yin, G.H., 2015. S-Pb isotopic geochemistry of Xiuwacu magmatic hydrothermal Mo-W deposit in Zhongdian area, NW Yunnan: constrains on the sources of metal. Acta Petrol. Sin. 31 (11), 3171–3188.

Wang, H., Wu, Y.-B., Gao, S., Qin, Z.-W., Hu, Z.-C., Zheng, J.-P., Yang, S.-H., 2016. Continental growth through accreted oceanic arc: zircon Hf–O isotope evidence for granitoids from the Qinling orogen. Geochim. Cosmochim. Acta 182, 109–130.

Wang, P., Dong, G.-C., Zhao, G.-C., Han, Y.-G., Li, Y.-P., 2018. Petrogenesis of the Pulang porphyry complex, southwestern China: implications for porphyry copper metallogenesis and subduction of the Paleo-Tethys Oceanic lithosphere. Lithos 304-307, 280–297.

Watson, E.B., Wark, D.A., Thomas, J.B., 2006. Crystallization thermometers for zircon and rutile. Contrib. Mineral. Petrol. 151 (4), 413–433.

Weislogel, A.L., 2008. Tectonostratigraphic and geochronologic constraints on evolution of the northeast Paleotethys from the Songpan-Ganzi complex, Central China. Tectonophysics 451 (1–4), 331–345.

Woodhead, J., Hergt, J., Shelley, M., Eggins, S., Kemp, R., 2004. Zircon Hf-isotope analysis with an excimer laser, depth profiling, ablation of complex geometries, and concomitant age estimation. Chem. Geol. 209 (1), 121–135.

Wu, W.H., Xu, S.J., Yang, J.D., Yin, H.W., Lu, H.Y., Zhang, K.J., 2010. Isotopic characteristics of river sediments on the Tibetan Plateau. Chem. Geol. 269 (3–4), 406–413.

Wu, T., Xiao, L., Wilde, S.A., Ma, C.Q., Zhou, J.X., 2017. A mixed source for the Late Triassic Garze-Daocheng granitic belt and its implications for the tectonic evolution of the Yidun arc belt, eastern Tibetan Plateau. Lithos 288, 214–230.

Yang, J.-H., Wu, F.-Y., Wilde, S.A., Xie, L.-W., Yang, Y.-H., Liu, X.-M., 2007. Tracing magma mixing in granite genesis: in situ U–Pb dating and Hf-isotope analysis of zircons. Contrib. Mineral. Petrol. 153 (2), 177–190.

Yang, L.Q., Deng, J., Dilek, Y., Meng, J.Y., Gao, X., Santosh, M., Wang, D., Yan, H., 2016. Melt source and evolution of I-type granitoids in the SE Tibetan Plateau: Late Cretaceous magmatism and mineralization driven by collision-induced transtensional tectonics. Lithos 245, 258–273.

Yin, A., Harrison, T.M., 2000. Geologic evolution of the Himalayan-Tibetan orogen. Annu. Rev. Earth Planet. Sci. 28, 211–280.

Zhu, Y.-S., Yang, J.-H., Sun, J.-F., Wang, H., 2017. Zircon Hf-O isotope evidence for recycled oceanic and continental crust in the sources of alkaline rocks. Geology 45 (5), 407–410.